

**RESEARCH ARTICLE**

10.1029/2024MS004693

**Key Points:**

- Mesoscale eddies sharpen a large-scale tracer front along the western boundary current extension
- The eddy-induced frontal sharpening can be described via an eddy-induced advection
- A functional form of the effective velocity can reproduce the frontal sharpening in a coarse-resolution tracer model

**Supporting Information:**

Supporting Information may be found in the online version of this article.

**Correspondence to:**

Y. Lu and I. Kamenkovich,  
yl24q@fsu.edu; ikamenkovich@miami.edu

**Citation:**

Lu, Y., & Kamenkovich, I. (2025). Mesoscale eddy-induced sharpening of oceanic tracer fronts. *Journal of Advances in Modeling Earth Systems*, 17, e2024MS004693. <https://doi.org/10.1029/2024MS004693>

Received 5 SEP 2024

Accepted 21 JAN 2025

# Mesoscale Eddy-Induced Sharpening of Oceanic Tracer Fronts

Yueyang Lu<sup>1,2</sup>  and Igor Kamenkovich<sup>1</sup> 

<sup>1</sup>Rosenstiel School of Marine, Atmospheric, and Earth Science, University of Miami, Coral Gables, FL, USA, <sup>2</sup>Center for Ocean-Atmospheric Prediction Studies, Florida State University, Tallahassee, FL, USA

**Abstract** Oceanic fronts are ubiquitous and important features that form and evolve due to multiscale oceanic and atmospheric processes. Large-scale temperature and tracer fronts, such as those found along the eastward extensions of the Gulf Stream and Kuroshio currents, are crucial components of the regional ocean environment and climate. This numerical study examines the relative importance of large-scale currents and mesoscale currents (“eddies”) in the front formation and evolution. Using an idealized model of the double-gyre system on both eddy-resolving and coarse-resolution grids, we demonstrate that the effect of eddies is to sharpen the large-scale tracer front, whereas the large-scale current counteracts this effect and acts to create a broader front. The eddy-driven frontogenesis is further described in terms of a recently proposed framework of generalized eddy-induced advection, which represents all those eddy effects on tracers that are not due to eddy-induced mass fluxes and are traditionally parameterized by isopycnal diffusion. In this study the generalized advection is formulated using an effective eddy-induced velocity (EEIV), which is the speed at which eddies move large-scale tracer contours. The advantage of this formulation is that the frontal sharpening can be readily reproduced by EEIVs. A functional form of EEIV in terms of large-scale variables effectively represents the frontogenesis in a coarse-resolution simulation. This study shows promise for using an advective framework to parameterize eddy-driven frontogenesis in numerical models that are not eddy-resolving.

**Plain Language Summary** Ocean fronts are characterized by sharp transitions in water properties (tracers). This study focuses on the formation of such elongated fronts, like the one along the Gulf Stream extension, which plays a crucial role in both regional and global climate. The primary focus is on the role of ocean mesoscale eddies, which are oceanic features spanning tens to hundreds of kilometers. We find that these eddies sharpen the front by moving tracers, while the large-scale current counteracts this effect. We developed a new method to describe these dynamics using so-called eddy-induced velocities, which represent the collective action of eddies on large-scale fronts. Our method successfully reproduces the formation and sharpening of a tracer front in a numerical ocean model with spatial resolution coarser than the oceanic mesoscale. The results of our study pave the way for accurately accounting for unresolved eddy effects on tracer fronts in climate models.

## 1. Introduction

Fronts, characterized by narrow bands of enhanced gradients of physical and biogeochemical tracers such as temperature, dissolved carbon and nutrients, are ubiquitous in the upper ocean. The width of ocean fronts can range from a few meters to tens of kilometers (McWilliams, 2021), and processes at various spatial scales play a role in front formation and evolution (Belkin et al., 2009). Fronts can facilitate the transfer of the tracers from the surface to the ocean interior and influence the climate and ocean ecological systems (D’Asaro et al., 2011; Ferrari, 2011; Lohmann & Belkin, 2014). The fronts associated with strong large-scale currents, such as western boundary current extensions and the Antarctic Circumpolar Current, can extend for hundreds of kilometers and are particularly important. These large-scale fronts can act as dynamical barriers to cross-frontal transport and mixing (Rypina et al., 2011, 2013) and impact the lower troposphere and mid-latitude climate (Minobe et al., 2008; Seo et al., 2023; Small et al., 2008). The goal of this study is to examine the role of ocean mesoscale eddies [length scale of  $O(10\text{--}100)$  km; “eddies” hereafter] in the evolution of large-scale temperature and tracer fronts associated with the eastward extensions of western boundary currents.

Oceanic mesoscale eddies pervade the vicinity of large-scale currents and the associated tracer fronts. Baroclinic instability of these currents, which is one of the main mechanisms for eddy generation, can be expected to weaken the vertical shear and density fronts (Pedlosky, 1987; Vallis, 2017). On the other hand, eddies can have a straining

**Table 1**  
*List of Acronyms Used in This Paper*

Parameter	Description
EEIV	Effective eddy-induced velocity, $\chi_{\perp}$
EIV	Eddy-induced velocity
ELSV	Effective large-scale velocity, $u_{\perp}$
GM	Gent and McWilliams (1990) parameterization
MOM6	Modular Ocean Model version 6
PV	Potential vorticity
RMS	Root mean square
SST	Sea surface temperature

effects that generate and sharpen the fronts (e.g., Berloff, 2005a; Waterman & Jayne, 2011). Oceanic components in modern climate models, however, do not fully resolve mesoscale eddies (Hewitt et al., 2020; Meijers, 2014), which leads to biases in the simulated ocean state. For example, non-eddy-resolving models produce significantly weaker sea surface temperature (SST; see Table 1 for the list of acronyms used in this paper) fronts in the Gulf Stream extension compared to those observed in eddy-resolving ocean models or observational data (Kirtman et al., 2012; Parfitt et al., 2016; Siqueira & Kirtman, 2016). The biases in the SST front in these simulations can impact the atmospheric temperature front (Parfitt et al., 2016), storm tracks (Small et al., 2014), and climate variability (Kirtman et al., 2012).

Mesoscale eddies can affect tracer fronts through three main types of processes: the dynamic feedback of eddies on the large-scale current, the advection of the large-scale tracer by eddy-induced mass fluxes, and the eddy tracer stirring along isopycnals. Most of previous studies have focused on

understanding and parameterization of the first two processes. The dynamic effect of eddies involves eddy-induced transfer of momentum (Waterman et al., 2011) and potential vorticity (PV; S. Bachman et al., 2017; Berloff, 2005a; Mana & Zanna, 2014; Rhines & Young, 1982; Ryzhov & Berloff, 2022; Waterman & Jayne, 2011), which can either dissipate or sustain the large-scale current, leading to changes in the tracer front. Progress has been made in understanding these dynamical effects (e.g., Berloff, 2005a; Shevchenko & Berloff, 2015; Uchida et al., 2022). For example, strengthening effect of eddies on large-scale currents is commonly associated with energy backscatter and a promising eddy “backscatter” scheme has been shown to energize the partially resolved eddies and, consequently, the large-scale currents in eddy permitting simulations (S. Bachman, 2019; Berloff, 2018; Grooms et al., 2015; Jansen & Held, 2014; Jansen et al., 2019; Yankovsky et al., 2024; Zanna et al., 2017).

The second effect, eddy-induced mass transport, generally acts to flatten isopycnals and is commonly parameterized by the Gent–McWilliams framework (“GM”, Gent & McWilliams, 1990; Gent et al., 1995). This effect has been extensively studied and recent efforts mostly focus on advancing the GM parameterization (e.g., S. Bachman, 2019; S. D. Bachman et al., 2020; Grooms, 2016; Grooms & Kleiber, 2019). One of the main advantages of the GM parameterization is its advective form, based on the GM eddy-induced velocities (EIV). These velocities represent advection of oceanic tracers by the eddy-induced mass transport.

The concept of EIV will be used in this study to represent the third process, eddy tracer stirring, which is the most direct effect of eddies on tracers. It is traditionally treated as an isotropic eddy-induced diffusion (Gent et al., 1995; Redi, 1982). However, several recent studies have revealed the importance of its anisotropic diffusive (S. Bachman et al., 2015; S. D. Bachman et al., 2020; Haigh et al., 2021b; Kamenkovich & Garraffo, 2022; Kamenkovich et al., 2021; W. Zhang & Wolfe, 2022) and advective (Haigh et al., 2021a; Lu et al., 2022) properties for tracer distributions. Most importantly, some of these studies of eddy diffusion demonstrate persistent up-gradient (negative) eigenvalues of a diffusion tensor, which implies tracer filamentation and frontal sharpening (“frontogenesis”; Haigh et al., 2020; Kamenkovich et al., 2021; Sun et al., 2021). Negative diffusivity, however, not only contradicts the conceptual analogy between turbulent and molecular diffusive mixing, but also leads to numerical instability in practical tracer simulations (Kamenkovich & Garraffo, 2022; Lu et al., 2022).

Recently, Lu et al. (2022) have proposed a generalized eddy-induced advection to quantify the direct eddy effects, and used it to successfully reproduce the eddy-induced stirring and dispersion in a high-resolution model. Though it has been known that spatially varying, nonlinear diffusivity can help generate fronts (e.g., Nakamura & Zhu, 2010), few has studied whether an advection can do the work. The eddy-induced advection is promising to be an appropriate model for the large-scale frontal development because the frontogenesis is essentially an advective process (McWilliams, 2021). In addition, the transport barriers associated with the fronts are expected to result from the joint action of the large-scale and eddy advections (Berloff et al., 2009; Kamenkovich et al., 2019). The advective formulation has a clear advantage over the diffusive framework in this regard. For example, a perfect transport barrier naturally results from the full cancellation between the large-scale and eddy-induced cross-barrier velocity (zero “residual velocity”). In contrast, such barrier would be challenging to reproduce by using purely diffusive representation of the eddy transport, because the required cancellation of the advective and

**Table 2**  
*List of Parameters Used in the High-Resolution Model*

Parameter	Value	Description
$L_x \times L_y$	$3840 \times 3840 \text{ km}$	Horizontal domain dimensions
$\Delta x$	$3.75 \text{ km}$	Horizontal fine grid spacing
$H_1, H_2, H_3$	$(0.3, 0.7, 3) \text{ km}$	Initial isopycnal layer thicknesses
$D$	$4 \text{ km}$	Ocean depth
$f_0$	$4.4 \times 10^{-5} \text{ s}^{-1}$	Coriolis parameter at the southern boundary
$\beta$	$2 \times 10^{-11} \text{ m}^{-1} \text{ s}^{-1}$	Meridional gradient of Coriolis parameter
$\rho_0$	$1035 \text{ kg m}^{-3}$	Reference density
$\nu$	$100 \text{ m}^2 \text{ s}^{-1}$	Horizontal Laplacian viscosity
$g$	$9.8 \text{ m s}^{-2}$	Gravity
$g'$	$(0.01, 0.0003) \text{ m s}^{-2}$	Reduced gravities at the upper interface of layer $k = 2, 3$
$Rd_1, Rd_2$	$(44, 25.3) \text{ km}$	First and second baroclinic Rossby deformation radii
$C_d$	0.003	Linear bottom drag coefficient
$ \mathbf{u}_* $	$0.1 \text{ m s}^{-1}$	Near-bottom velocity magnitude
$\tau_0$	$0.22 \text{ N m}^{-2}$	Wind stress amplitude
$r$	$2 \times 10^{-8} \text{ s}^{-1}$	Relaxation rate for the upper layer thickness
$\kappa_{tr}$	$100 \text{ m}^2 \text{ s}^{-1}$	Background isopycnal tracer diffusivity

diffusive fluxes cannot be guaranteed for an arbitrary tracer. This study will build upon the approach of Lu et al. (2022), examining how effectively the stirring effects of eddies on a large-scale front can be modeled by eddy-induced advection and expressed by large-scale quantities, potentially leading to an effective parameterization.

The paper is organized as follows. Section 2 describes the ocean models and tracer simulations used in this study. Section 3 derives the tracer eddy forcing that includes the effects of eddies on a large-scale front, the frontogenesis equation and the generalized advective model of the eddy forcing. Section 4 examines the eddy effects on the front via the analyses of the frontogenesis equation and the eddy-induced velocity. Section 5 discusses performance of the tracer simulations with the eddy-induced advection. Section 6 offers conclusions.

## 2. Model and Simulations

In this section we describe tracer simulations in idealized primitive-equation models. The dynamical setting is described in Section 2.1, where we also briefly compare simulated flows at high resolution (3.75 km) and low resolution (60 km) settings. The drastic difference in the eastward jet properties between the two simulations would make it challenging to isolate the impact of eddy tracer stirring on the tracer front. This challenge motivates us to use the flow from the high-resolution simulation, projected onto the coarse grid, to advect tracers. The tracers are described in Section 2.2. The tracer simulations advected by the projected high-resolution flow, as elaborated in Section 2.3, will be used throughout the rest of the paper. We will see that, despite having “perfect” large-scale mass fluxes, these simulations still exhibit biases in the tracer fields unless the eddy tracer stirring effects are included.

### 2.1. Primitive Equation Ocean Model

We use the Modular Ocean Model version 6 (MOM6, Adcroft et al., 2019) to solve the adiabatic shallow-water equations in a square basin with flat bottom. The model represents a wind-driven mid-latitude, double-gyre ocean circulation in the Northern Hemisphere, whose setup is motivated by Cooper and Zanna (2015). The model has three stacked isopycnal layers with a free surface. Key parameters are summarized in Table 2.

Detailed description of MOM6 equations can be found in Yankovsky et al. (2022) and C. Zhang et al. (2023). Here we briefly repeat them. The momentum and continuity equations in layer  $k$  ( $k = 1, 2, 3$  with  $k = 1$  denoting upper layer) are

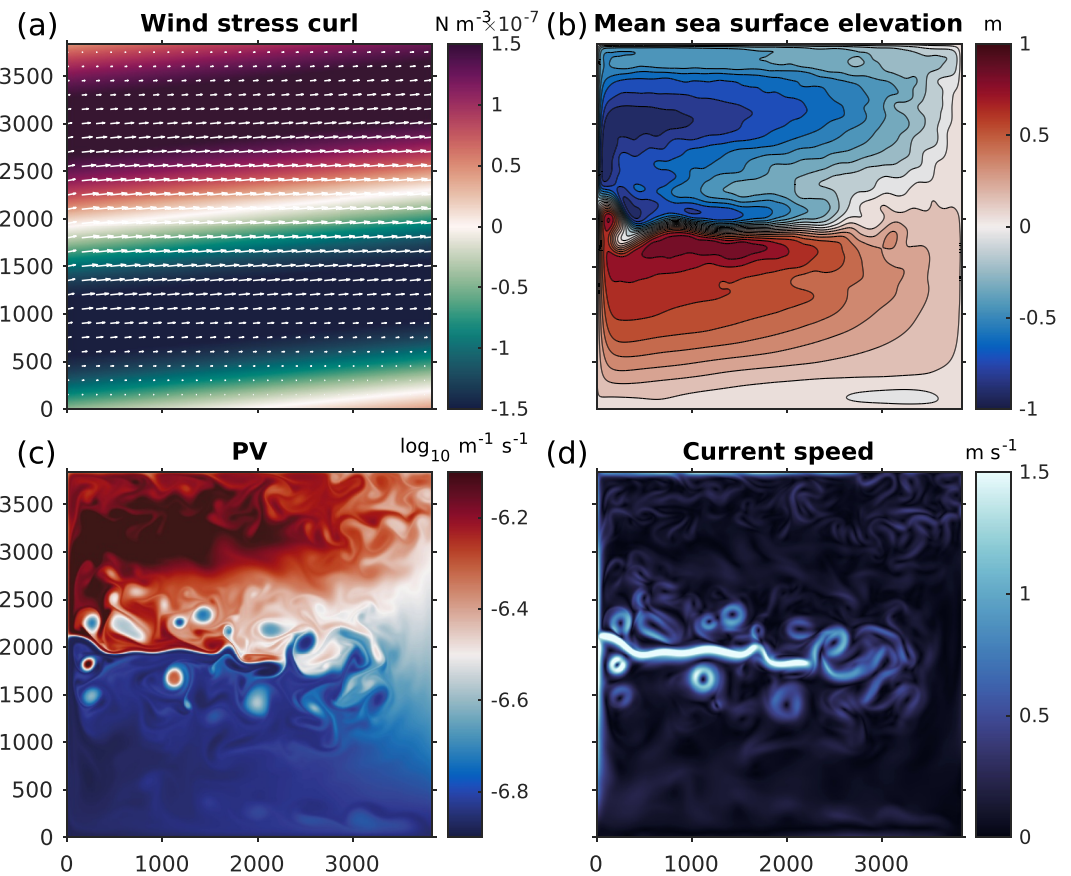


**Figure 1.** High-resolution simulations. (a) Wind stress vector and its curl. (b) Sea surface elevation averaged from year 21 to year 23. Snapshots of (c) potential vorticity and (d) current speed at day 120 years 21. All fields are in the upper layer.

$$\frac{\partial \mathbf{u}_k}{\partial t} + \frac{f + \zeta_k}{h_k} \hat{\mathbf{z}} \times (\mathbf{u}_k h_k) + \nabla \left( M_k + \frac{|\mathbf{u}_k|^2}{2} \right) = \delta_{1k} \frac{\boldsymbol{\tau}}{\rho_0 h_1} - \delta_{3k} \frac{C_d}{h_k} |\mathbf{u}_*| \mathbf{u}_k + \nabla \cdot \boldsymbol{\sigma}_k, \quad (1a)$$

$$\frac{\partial h_k}{\partial t} + \nabla \cdot (\mathbf{u}_k h_k) = R_h(h_k). \quad (1b)$$

where  $\mathbf{u}_k$  is the horizontal velocity,  $f = f_0 + \beta y$  is the planetary vorticity following the beta-plane approximation,  $\zeta_k = \hat{\mathbf{z}} \cdot \nabla \times \mathbf{u}_k$  is the vertical component of relative vorticity,  $\hat{\mathbf{z}}$  is the unit vector in the vertical direction,  $h_k$  is layer thickness,  $\delta_{ij}$  is the Kronecker delta, and  $\nabla$  is the horizontal (isopycnal) gradient. The Montgomery potential  $M_k$  is

$$M_k = \sum_{i=1}^k g'_{i-1/2} \eta'_{i-1/2}, \quad (2)$$

where  $g'_{i-1/2}$  is the reduced gravity at the upper interface of layer  $k$  and its value is prescribed (Table 2) so that the first and second baroclinic Rossby deformation radii are  $Rd_1 = 44$  km and  $Rd_2 = 25.3$  km, respectively, and the upper interface height of layer  $k$  is  $\eta'_{k-1/2} = -D + \sum_{i=1}^k h_i$ . The bottom stress is calculated from a linear drag law that depends on a prescribed near-bottom flow speed  $|\mathbf{u}_*|$  and coefficient  $C_d$ . The horizontal and vertical stress tensor  $\boldsymbol{\sigma}_k$  is parameterized by Laplacian viscosity. With this choice of the lateral Laplacian viscosity the Munk layer is well resolved with 4 grid points. We also tried smaller values and obtained similar flow fields.

The steady, asymmetric, and tilted wind stress  $\tau$  (Figure 1a), used in numerous studies (e.g., Berloff, 2015; Haigh & Berloff, 2021; Haigh et al., 2020), is

$$\tau_x = \frac{\tau_0}{2} \left[ 1 + \cos \left( \frac{2\pi(mx - y + L_y/2)}{(1+m)L_y} \right) \right], \quad (3a)$$

$$\tau_y = m\tau_x, \quad (3b)$$

where the tilt parameter  $m = 0.1$ . A relaxation term  $R_h(h_k) = \delta_{lk}r(h_r - h_k)$  is applied to the upper layer thickness (1b). The reference profile is the initial layer thickness  $H_1$  plus a sinusoidal profile whose zero-crossing line overlaps the zero wind stress curl line:

$$h_r = H_1 + \Delta h \sin \left( \frac{2\pi(mx - y + L_y/2)}{(1+m)L_y} \right), \quad (4)$$

with  $\Delta h = 150$  m. The relaxation is added to maintain a basin-wide isopycnal (thermocline) slope, mimicking air-sea buoyancy exchanges that have the same effect in the real ocean. The isopycnal slope is a key parameter for baroclinic instability, as it provides the available potential energy that drives these instabilities. Our analysis further shows that the relaxation indeed helps to maintain the realistically vigorous eddy field which sustains a coherent eastward extension of the boundary current. Notably, the relaxation to the large-scale profile does not directly induce the jet extension. The relaxation is also verified not to affect the net mass balance.

The square domain ( $L_x \times L_y = 3,840$  km  $\times$  3,840 km) is closed by solid boundaries, where free slip and no normal flux boundary conditions are applied. The equations are discretized on a uniform high-resolution (eddy-resolving) grid of 3.75 km resolution ( $1024^2$  grid cells) with a time step of 50 s.

The model is spun up for 20 years from the state of rest to reach a statistically steady flow. It is then run for 2 additional years with all model fields saved every 6 hr as both the 6-hr averaged quantities and snapshots. Figures 1b–1d show the ocean circulation in the eddy-resolving simulation. The model develops a strongly eddying double-gyre flow, separated by a meandering jet extending from the western boundary and representing the Gulf Stream or Kuroshio extension. This eastward jet extension will be simply referred to as “jet” hereafter. A near-zonal front of PV, characterized by large meridional PV gradients, is formed along the jet (Figure 1c).

For comparison, we also perform a coarse-resolution simulation on a grid of 60 km resolution ( $64^2$  grid cells), where eddies are not fully resolved and the large-scale current is not simulated accurately. The grid resolution is coarser than the second baroclinic deformation radius (25.3 km) and is between what is usually referred to as “coarse resolution” ( $>1$  deg) and “eddy-permitting” ( $\sim 25$  km) regimes. It can be relevant to the latter regime due to the presence under-resolved mesoscale features (fronts and meanders). We call it “intermediate resolution” to avoid confusion. The eddy effects on momentum and density are represented by Laplacian momentum dissipation with a dimensionless Smagorinsky coefficient (Griffies & Hallberg, 2000) of 0.15 and the GM scheme (Gent et al., 1995) with a constant GM parameter of  $400 \text{ m}^2 \text{ s}^{-1}$ , respectively. The value of GM diffusivity used here is a common choice typical for mid-latitude ocean, and the Smagorinsky coefficient is similar to that used in Marques et al. (2022).

The simulated fields exhibit large biases in the position and intensity of the jet and the associated tracer front because of the under-represented eddy effects on dynamics and density. Figure 2a shows the residual velocity from the coarse-resolution simulation: the sum of the large-scale velocity solved by the model and the eddy-induced velocity as parameterized by the GM scheme. The jet barely extends eastward and occupies a different position compared to the high-resolution model (Figure 1d). We attempted several other constant values of these parameters and observed similar results. We did not, however, explore the full range of options with different schemes and non-constant coefficients. Promising new approaches such as the eddy backscatter scheme and stochastic parameterizations can re-energize the flow and reduce the bias due to the eddy dynamic effect in coarse-resolution models (S. Bachman, 2019; Grooms, 2023; Jansen et al., 2019; Yankovsky et al., 2024; Zanna et al., 2017), but they are not considered here.

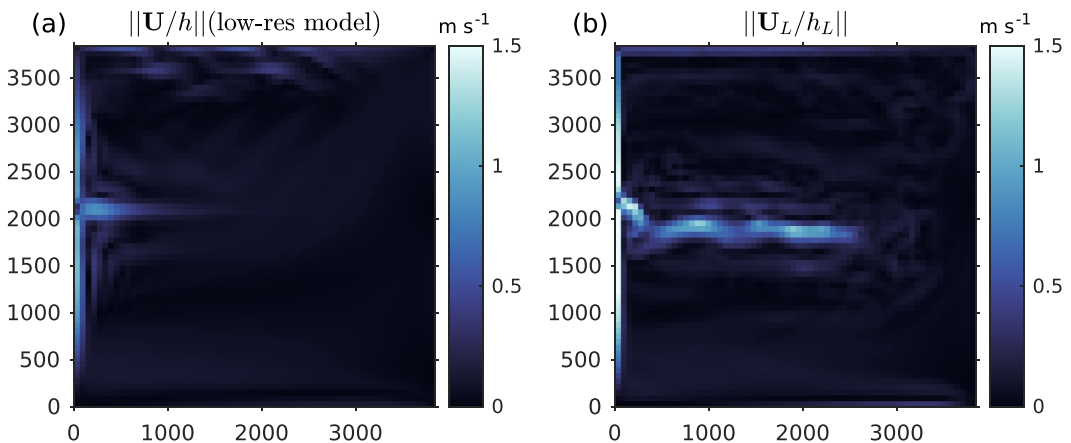


**Figure 2.** (a) The residual velocity speed (large scale plus GM velocities) simulated in the coarse-resolution model. (b) The residual velocity speed coarse-grained from the high-resolution (eddy-resolving) model solution. It is defined in Section 3.1. All fields are diagnosed at day 120 years 21 in the upper layer. Note that in this study we use (b) to advect tracers.

As explained at the beginning of Section 2, we will use the projection of high-resolution mass fluxes onto the coarse grid to advect tracers (described below) throughout the rest of this study. The low-resolution simulations discussed in this subsection will not be used further.

## 2.2. Tracers Used in This Study

The evolution of tracer concentration  $c$  in each layer on the high-resolution grid is governed by

$$\frac{\partial(hc)}{\partial t} + \nabla \cdot (\mathbf{U}c) = \nabla \cdot (\kappa_{tr} h \nabla c) + R_{tr}(c) \quad (5)$$

where  $\mathbf{U} = \mathbf{uh}$  is the horizontal mass flux,  $R_{tr}(c) = r_{tr}h(c_r - c)$  is a relaxation of the tracer back to its initial distribution  $c_r$ ,  $r_{tr}$  is the relaxation rate, and the layer subscript is omitted hereafter. The relaxation is applied in the upper layer only and is intended to mimic interactions with the atmosphere and prevent the tracer field from rapid homogenization. We set the subgrid tracer diffusivity  $\kappa_{tr} = 100 \text{ m}^2 \text{ s}^{-1}$  for all tracer simulations in this study. Tracers are initialized on the first day of year 21 and are simulated for 2 years. We confirmed that the tracer concentration has reached equilibrium after about 200 days based on the domain-averaged tracer variance. Note that this study is concerned with the formation of the front, and does not employ long-term time averaging. Thus, a 2-year tracer simulation is sufficient for our analysis.

We consider two idealized tracers initialized with meridional profiles, that are vertically and zonally uniform. For the robustness of the conclusions, we chose tracers with very different spatial distributions, both relevant to the real ocean properties. One tracer has an initial southward gradient (values increasing from north to south) generally consistent with the observed annual-mean SST, and a relaxation time scale of  $1/r_{tr} = 400$  days that mimics the dependence of the surface heat flux on SST (Haney, 1971), given the average thickness of our top layer of 300 m. We call it a “passive temperature” tracer. The other has an initial northward gradient (values increasing south to north) that is typical of chemical tracers with higher solubility at cold temperatures such as CFC-11. It has a relaxation time scale of 125 days that mimics the time scale associated with the gas transfer of CFC-11 with the atmosphere (England et al., 1994). We call it a “chemical” tracer. Despite having initial profiles analogous to realistic SST and CFC-11, these idealized tracers should not be interpreted as realistic simulations of these real-ocean properties. For additional analysis of the sensitivity of the results to tracers, we will also use eight additional color-dye tracers with initial linear and sinusoidal distributions (Supporting Information S1).

Figure 3 shows the initial profiles and subsequent solutions in the high-resolution model. For the passive temperature, the western boundary currents bring warm (cold) water from subtropical (subpolar) gyre to the latitude of the jet ( $y \approx 2,000 \text{ km}$ ), where the warm and cold currents meet and continue eastward. This confluence of cold and warm waters creates a sharp temperature front along the jet extension. The warm and cold waters retain their

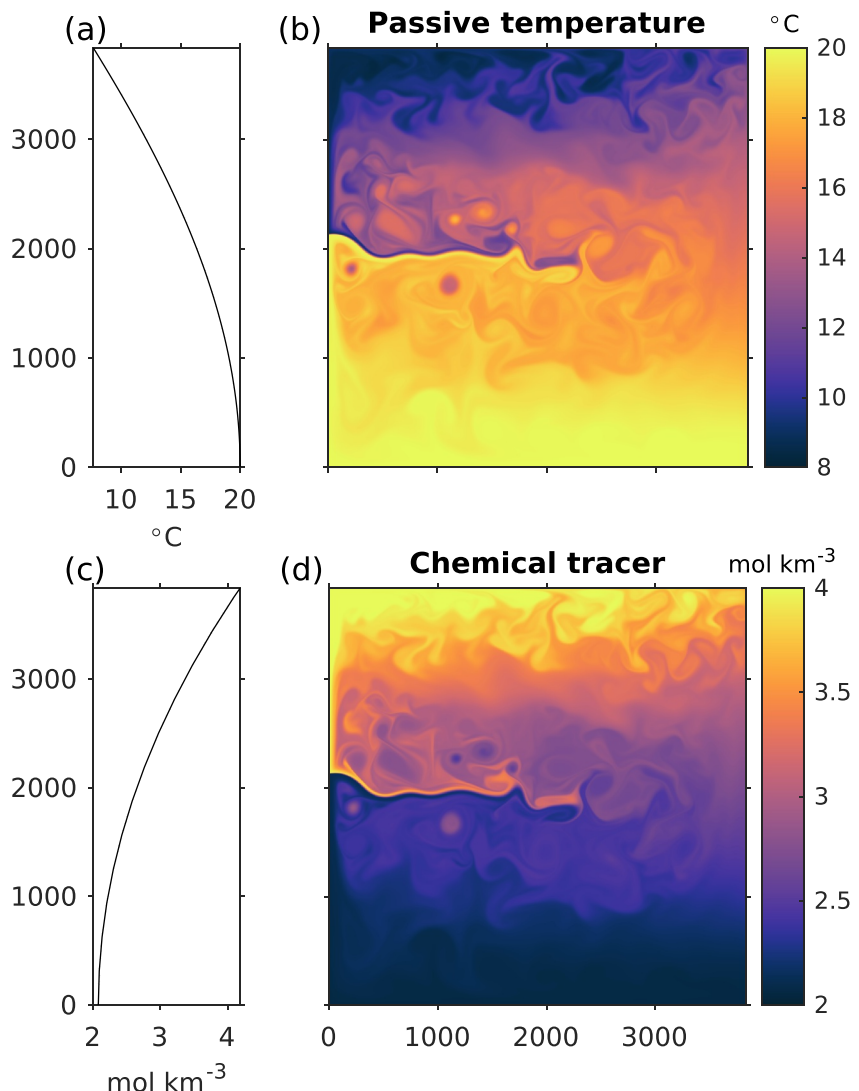


**Figure 3.** (a) Initial meridional profile and (b) upper layer tracer solution at day 120 years 21 for the passive temperature tracer. (c)–(d) Same but for the chemical tracer.

temperature contrast, avoiding strong mixing with each other and indicating presence of an at least partial mixing barrier along the jet axis (Dritschel & McIntyre, 2008; Kamenkovich et al., 2019; Rypina et al., 2011, 2013). Similar features are observed for the chemical tracer, except that the front is characterized by large northward meridional gradient.

### 2.3. Coarse-Resolution Tracer Simulations

The focus of this study is on the effect of mesoscale eddies on a large-scale tracer front. For this purpose, we perform tracer simulations on the coarse-resolution grid:

$$\frac{\partial(h_L c_L)}{\partial t} + \nabla_c \cdot (\mathbf{U}_L c_L) = \nabla_c \cdot (\kappa_{tr} h_L \nabla_c c_L) + R_{tr}(c_L) + \mathcal{D} \quad (6)$$

where the subscript  $L$  denotes the large-scale fields,  $\nabla_c$  is a horizontal gradient on the coarse grid, and  $\mathcal{D}$  is a term representing subgrid eddy effects.  $h_L$  is a large-scale layer thickness whose equation will be given later.  $\mathbf{U}_L$  is a large-scale mass flux (flow) defined on the coarse grid.

**Table 3**  
*Coarse-Grid Tracer Experiments Performed in This Study*

Name	Description
NO_EF	Experiment without eddy forcing
FULL_EF	Experiment with the eddy forcing of full spatiotemporal variability
FULL_EEIV	Experiment with the diagnosed EEIV of full spatiotemporal variability
FUN_EEIV	Experiment with the proposed functional form of EEIV

The spatial resolution of the coarse grid (60 km), which is in the “intermediate resolution” regime, is sufficient to detect a tracer front but too coarse to accurately simulate its dynamics. The grid spacing is slightly shorter than the width of the tracer front in the high-resolution model. The latter width is  $O(100 \text{ km})$ , as estimated from the meridional tracer gradient, and cannot be resolved at the coarse resolution. Our goal is, therefore, to reproduce the large-scale component  $c_L$  of the full (high-resolution) tracer concentration  $c$ , which can be adequately resolved on the 60 km grid. The exact definition of this component will be given in the next section.

As discussed above, eddies can affect the large-scale tracer concentration through three pathways: (a) the dynamical modulation of the large-scale (Eulerian) velocity  $\mathbf{u}$  solved in Equation 1a; (b) the eddy-induced mass/density transport  $\mathbf{U}_L - \mathbf{u}h_L$  that affects  $h_L$  in Equation 1b and tracer in Equation 6; and (c) the direct eddy stirring effects  $D$ . The coarse-grid tracer solution will be different from the fine-grid tracer unless all three eddy effects are represented accurately.

In the context of the passive tracer model (Equation 6) alone,  $\mathbf{U}_L$  is an external variable that can be set to any meaningful field. There are two physically meaningful ways to obtain  $\mathbf{U}_L$ : as a solution of the momentum equations on the coarse grid in the low-resolution model, that is, the flow in Figure 2a; or as a low-pass filtered (“coarsened”) high-resolution model solution  $\mathbf{U}$ .

As discussed above, we focus on the direct stirring effect of eddies (term  $D$ ) and choose the latter option to derive  $\mathbf{U}_L$ . This choice ensures that the coarse-grid tracer is advected by the “correct” residual flow  $\mathbf{U}_L$ , without enduring extra biases resulting from the parameterizations of the eddy effects on momentum and density. This approach also allows us to demonstrate that even a “full” residual mass transport from the high-resolution simulation is not sufficient to produce a realistic tracer front on a coarse grid.

We employ the offline method that uses pre-calculated mass flux and layer thicknesses to solve the tracer Equation 6 on the coarse grid. The method has been used for studies on the importance of mesoscale currents in tracer transports (Kamenkovich & Garraffo, 2022; Kamenkovich et al., 2017, 2021) and the representation of eddy-induced advection and diffusion (Lu et al., 2022). We perform four offline tracer experiments with different forms of the eddy term  $D$  in this study. They are listed in Table 3 and will be explained in following sections.

To ensure that there are no spurious sources of tracer mass, the large-scale layer thickness needed in (6) is solved from the continuity equation on the coarse grid, using prescribed large-scale mass fluxes:

$$\frac{\partial h_L}{\partial t} + \nabla_c \cdot \mathbf{U}_L = R_h(h_L), \quad (7)$$

where the relaxation rate of the top layer thickness has the same value as the high-resolution model. The continuity and tracer time steps on coarse grid are 600 s. We also estimated the errors due to the offline calculations of tracer flux divergence, by comparing online and offline simulations of the passive temperature tracer (Supporting Information S1). We confirmed that the errors are sufficiently small to warrant the use of the offline method for passive tracer simulations.

### 3. Tracer Eddy Forcing and Frontogenesis Equation

In this section, we define the eddy forcing that represents the net eddy effects on the tracer, derive the equation for the meridional tracer gradient that governs the evolution of the jet front, and briefly discuss the generalized

advection model by Lu et al. (2022) that will be used to model the diagnosed eddy forcing in non-eddy-resolving simulations.

### 3.1. Tracer Eddy Forcing

A non-eddy-resolving tracer model needs a subgrid tracer “forcing” to account for the cross-scale transfer of tracer concentration and its variance due to mesoscale eddies (e.g., Haigh & Berloff, 2021). We define the tracer eddy forcing as the source term that augments the coarse-grid tracer solution toward a reference “truth” ( $c_L$ ), given a particular large-scale reference flow ( $\mathbf{U}_L$ ) on the coarse grid (Agarwal et al., 2021; Berloff et al., 2021). Note that in this definition, the eddy forcing is a function of the large-scale reference tracer  $c_L$  and mass transport  $\mathbf{U}_L$  fields. The tracer eddy forcing includes all the effects of unresolved eddies on tracer evolution, and this is precisely the term that needs to be analyzed and “parameterized”, in terms of large-scale properties, in the coarse-grid model (6). Such definition of the effects of unresolved-scale process has been widely used in the subgrid parameterization studies in both ocean (e.g., Agarwal et al., 2021; Berloff et al., 2021; Mana & Zanna, 2014; Ross et al., 2023; Uchida et al., 2022; Zanna & Bolton, 2020) and atmosphere (e.g., Wang et al., 2022; Yuval & O’Gorman, 2023). The approach has two main advantages over more traditional use of tracer fluxes (e.g., Lu et al., 2022): it can incorporate all eddy-related terms in the tracer budget and can mitigate ambiguity associated with large non-divergent (“rotational”) fluxes (Haigh et al., 2020; Kamenkovich et al., 2021; Lu et al., 2022; Maddison et al., 2015; Marshall & Shutts, 1981).

Equation 6 provides the definition of eddy forcing, after rearranging terms to one side:

$$D_e(\mathbf{U}_L, c_L) = \frac{\partial(h_L c_L)}{\partial t} + \nabla_c \cdot (\mathbf{U}_L c_L) - \nabla_c \cdot (\kappa_{tr} h_L \nabla c_L) - R_{tr}(c_L), \quad (8)$$

as long as that the large-scale reference flow and tracer are prescribed.

At this point, the entire coarse-resolution system (Equations 6–8) hinges on the definitions of the reference fields  $\mathbf{U}_L$  and  $c_L$ . We choose to define both variables from high-resolution model fields:

$$\mathbf{U}_L = \langle \mathbf{U} \rangle, \quad c_L = \langle c \rangle, \quad (9)$$

where the low-pass filtering (denoted by angle bracket) is a combination of spatial averaging over all fine-grid cells within a coarse-grid cell of 60 by 60 km (16 by 16 fine-grid cells) and time smoothing with a 180-day sliding average. The combination of spatial coarsening and time filtering removes the mesoscale variability more effectively than the spatial smoothing or time averaging alone, because mesoscale eddies are characterized by both spatial and temporal variabilities (Berloff & Kamenkovich, 2013; Capet et al., 2008; Kamenkovich & Garraffo, 2022). The decision to use a 180-day sliding window is based on the fact that the eddy time scale spans several months. We also tested a 2-year time average and confirmed that it does not change our conclusions in this study.

To make sure that the divergence of high-resolution mass flux  $\mathbf{U}$  is preserved on the coarse grid, we decompose  $\mathbf{U}$  into its divergent and rotational components and then coarse grain them separately. The derived  $\mathbf{U}_L$  is shown in Figure 2b. It retains the intensity and position of the jet in the high-resolution model, as well as preserving the mass flux divergence. Further details on this method and rationale are given in Appendix A.

Note that the eddy forcing (Equation 8) is equivalent to the commonly used definition that is obtained by low-pass filtering the high-resolution tracer Equation 5 and subtracting the result from the coarse-grid tracer Equation 6 (e.g., Mana & Zanna, 2014). This gives

$$D_e = \frac{\partial(h_L c_L)}{\partial t} - \langle \frac{\partial(hc)}{\partial t} \rangle + \nabla_c \cdot (\mathbf{U}_L c_L) - \langle \nabla \cdot (\mathbf{U}c) \rangle + \langle \nabla \cdot (\kappa_{tr} h \nabla c) \rangle - \nabla_c \cdot (\kappa_{tr} h_L \nabla c_L) + \langle R_{tr}(c) \rangle - R_{tr}(c_L). \quad (10)$$

The above equation is the same as Equation 8, given the fact that the high-resolution tracer Equation 5 as well as its low-pass filtered version is an equity at every instant. That is, the sum of all the terms in angle brackets  $\langle \rangle$  in Equation 10 is zero.

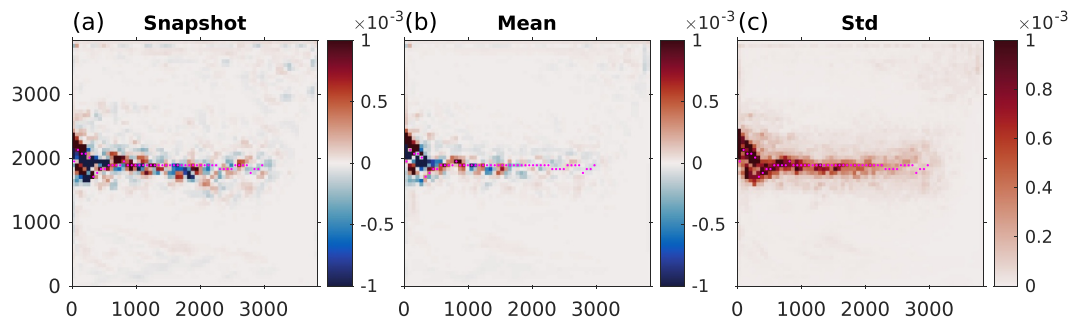


**Figure 4.** Eddy forcing for the passive temperature tracer. (a) Snapshot at day 361 years 21, (b) time-mean and (c) standard deviation over 2 years (years 21–22). Units are  $[{}^{\circ}\text{C m s}^{-1}]$ . Magenta dots are the jet core defined by the maximal speed of the large-scale (“residual”) velocity  $\mathbf{u}_L$  in the jet region ( $0 < x < 3000$  km,  $1600 < y < 2400$  km). All fields are in the upper layer.

Note that our definition of the eddy forcing (Equation 8) is generic and the large-scale flow  $\mathbf{U}_L$  and reference large-scale tracer  $c_L$  are independent of each other in this formulation. In other words,  $D_e$  can be calculated for any desired distribution  $c_L$  for any given  $\mathbf{U}_L$ . To check the robustness of the conclusions in the following analysis, we also calculated the eddy forcing for  $c_L$  defined as the spatially coarsened field, without any time filtering. The analysis led us to the same conclusions as in the default definition of  $c_L = \langle c \rangle$ .

The diagnosed eddy forcing  $D_e$  has complex spatiotemporal structure (Figures 4a–4c). Its largest values are concentrated along the jet, where eddies cause significant redistribution of the large-scale tracer. The standard deviation in  $D_e$  exceeds its time-mean in most of the domain, indicating significant time variability in the eddy activity. During the application of the diagnosed eddy forcing to the coarse-resolution tracer model, we found that additional correction is needed to compensate for numerical errors in calculating the eddy forcing, mainly arising from time sampling rate. Otherwise, these errors can grow causing the solution to diverge from  $\langle c \rangle$ . The eddy forcing in this paper includes the correction, which is small compared to the original eddy forcing, with an area r. m.s. value of approximately 6% of  $D_e$ , and does not affect the statistical structure of  $D_e$ . See Appendix B for more detail and a demonstration that  $D_e$  indeed augments the coarse-grid solution toward the reference “truth”  $\langle c \rangle$ .

To demonstrate the importance of eddies in the large-scale tracer distribution, we ran an experiment with  $D = 0$  (NO\_EF, Table 3) in which the eddy forcing is set to zero, and an experiment with  $D = D_e$  (FULL\_EF) in which the full eddy forcing is applied. Figures 5a and 5b compare the passive temperature solutions from the two experiments. The most important difference is in the vicinity of the front along the jet. The water is cooler (warmer) to the south (north) of the jet core in NO\_EF than in FULL\_EF, leading to a significantly weaker temperature front. We quantify the strength of the front by three metrics: the tracer gradient norm averaged in the jet region (Figure 5d), the tracer difference between the south and north of the jet (Figure 5e), and the meridional tracer profiles across the jet (Figure 5f). All three metrics show a significantly weaker front in the absence of eddy stirring in NO\_EF, despite using the accurate full (“residual”) mass flux  $\mathbf{U}_L$  that includes the eddy-induced mass transport. We see that the gradient norm in FULL\_EF is about 30% larger, and the temperature difference is about 0.8° (40%) higher than in NO\_EF. The meridional profiles also show sharper tracer gradients at different longitudes of jet in FULL\_EF than NO\_EF. This is a direct evidence that mesoscale eddies sharpen the front, a phenomenon that will be further substantiated in the subsequent sections. Note that the frontal sharpening is consistent with the theory of suppressed mixing in regions with strong PV gradients such as the jet region (Dritschel & McIntyre, 2008), which leads to the front being a transport barrier.

### 3.2. Frontogenesis Equation

To explore the eddy-driven sharpening of the jet front (“frontogenesis”), we derive the equation governing the evolution of tracer gradient on the coarse grid. We first combine the coarse-grid tracer budget (Equation 6) and the continuity (Equation 7) to get the advective form of the tracer equation:

$$\frac{\partial c_L}{\partial t} + \mathbf{u}_L \cdot \nabla_c c_L = \frac{D}{h_L} + \frac{\nabla_c \cdot (\kappa_{tr} h_L \nabla_c c_L)}{h_L} + \frac{R_{tr}(c_L) - c_L R_h(h_L)}{h_L} \quad (11)$$

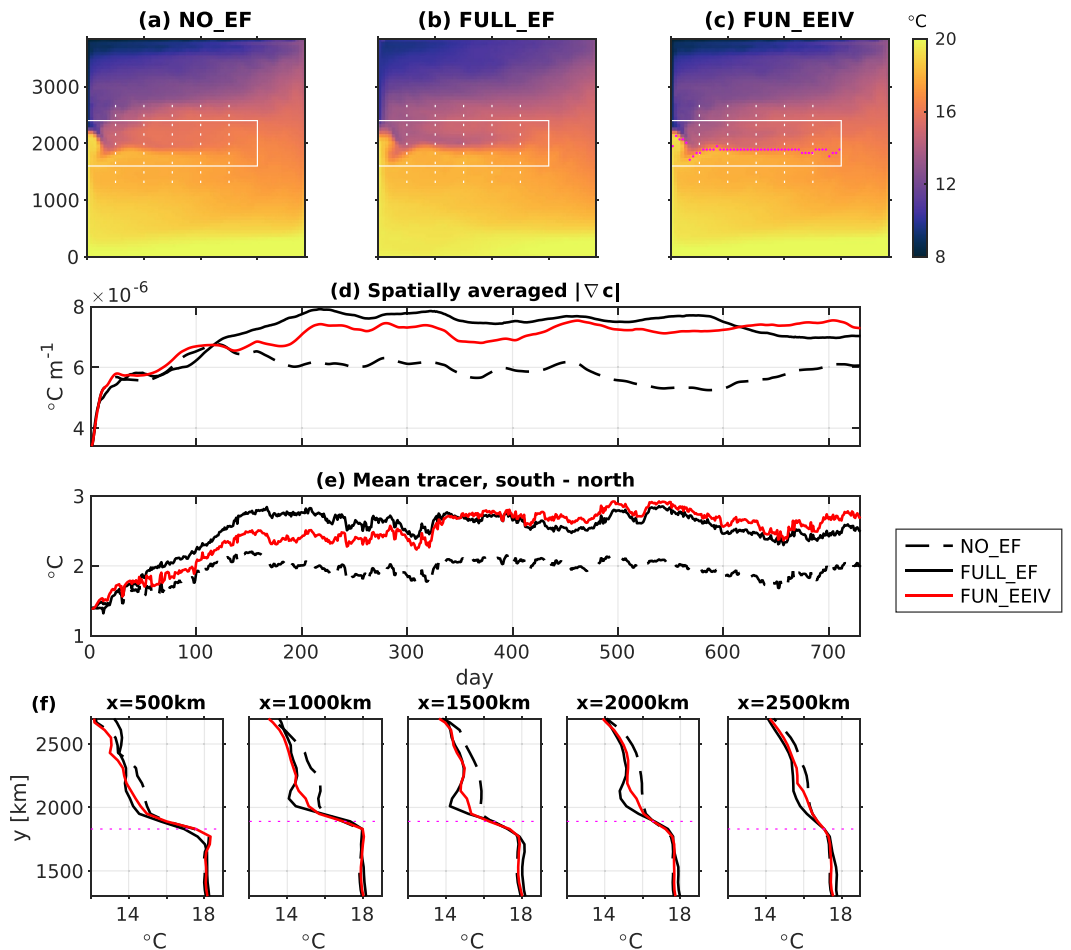


**Figure 5.** Passive temperature tracer solutions and front magnitudes in different experiments. Time-averaged solutions from the (a) NO\_EF, (b) FULL\_EF, and (c) FUN\_EEIV experiments over 2 years (year 21–22). Solid white lines are the boundaries of the jet region in which the spatial average is performed. Zonal magenta dots are the jet core that divides the jet region into the “north-of-jet” and “south-of-jet” region. Meridional dotted lines show the longitudes at which the profiles are diagnosed. (d) The tracer gradient norm averaged in the jet region. (e) The difference between the tracer inventory area-averaged in the south-of-jet and north-of-jet regions. (f) The meridional profiles of the tracer averaged over year 22 in all three experiments. All fields are in the upper layer.

where  $\mathbf{u}_L = \mathbf{U}_L/h_L$  is the large-scale (residual) velocity that includes the effect of eddy-induced mass flux. Due to the beta-effect, tracer gradients along the near-zonal jet front are nearly meridional, and we focus our analysis on the meridional direction. Applying  $[(\partial_y c_L)\partial_y]$  to Equation 11, we arrive at the equation of the (squared) meridional tracer gradient (a.k.a. frontogenesis equation; Hoskins, 1982; McWilliams, 2021; Mudrick, 1974):

$$\begin{aligned} \frac{\partial}{\partial t} (\partial_y c_L)^2 &= L + E + A + R, \\ L &= -2(\partial_y c_L)\partial_y(\mathbf{u}_L \cdot \nabla_c c_L), \\ E &= 2(\partial_y c_L)\partial_y(D/h_L), \\ A &= 2(\partial_y c_L)\partial_y(\nabla_c \cdot (\kappa_{tr} h_L \nabla_c c_L)/h_L), \\ R &= 2(\partial_y c_L)\partial_y((R_{tr}(c_L) - c_L R_h(h_L))/h_L). \end{aligned} \quad (12)$$

Here  $L$  describes the effects of the large-scale advection which consist of two distinct mechanisms: (a) the large-scale advection of the squared tracer gradient  $L_{adv} = -\mathbf{u}_L \cdot \nabla_c (\partial_y c_L)^2$  and (b) the confluence (strain) of large-scale velocity  $L_{con} = -2(\partial_y c_L)(\partial_y \mathbf{u}_L \cdot \nabla_c c_L)$ , where  $\partial_y \mathbf{u}_L$  is the meridional velocity gradient tensor.  $E$  is the

eddy effect on the tracer gradient, and  $A$  and  $R$  represent the effects of subgrid diffusion and relaxations, respectively.

### 3.3. The Generalized Advective–Diffusive Model

For an approximation  $\hat{D}_e$  of the full eddy forcing  $D_e$ , we use a generalized advective–diffusive framework recently proposed by Lu et al. (2022). The approximation will prove to be a convenient framework for a functional form representing eddy-driven frontogenesis. Here we present only a brief overview, and the reader is referred to Lu et al. (2022) for the full derivation.

The framework operates under the assumption that the effects of eddies on tracers can be depicted by a blend of diffusion and advection. In the most general form, the diffusive effects are represented by a 2D diffusivity tensor. The advective part includes terms representing spatial gradients of diffusivity tensor, advective (anti-symmetric) component of the transport tensor and a new EIV term  $\mathbf{U}_\chi$  (see below). Note that the advection here does not include the GM advection since they represent different eddy processes. This general formulation is not practical due to a large number of space- and time-dependent parameters that ultimately must be determined from large-scale properties in a parameterization closure.

In its reduced version, the framework represents the eddy forcing as a sum of isotropic, spatially inhomogeneous and time-dependent diffusion and advection by the generalized eddy-induced velocity (EIV):

$$\hat{D}_e = \kappa h_L \nabla_c^2 c_L - \chi \cdot h_L \nabla_c c_L, \quad (13)$$

where  $\kappa$  is an isotropic eddy diffusivity, and the generalized EIV  $\chi$  includes two advective eddy effects: the eddy-induced advection  $\mathbf{U}_\chi$  and the spatial gradient of diffusivity  $\nabla_c \kappa$ , arising from splitting the diffusion term:  $\nabla_c \cdot \kappa h_L \nabla_c c_L = \kappa h_L \nabla_c^2 c_L + \nabla_c \kappa \cdot h_L \nabla_c c_L$ . Both  $\kappa$  and  $\chi$  are *independent* parameters, to be determined from the full solution and parameterized in an effective closure. The generalized EIV  $\chi$  is separate from the GM velocity, and can be added to the latter in practical applications. In this study, we will use this approach to explore the advective effects of eddies on frontal evolution in a coarse-resolution model. As we will observe in the subsequent sections, the explicit formulation of the advective effects in Equation 13 simplifies its parameterization in simulations that do not resolve eddies.

In frontal zones, the advective velocities  $\mathbf{u}_L$  and  $\chi$  tend to be large and nearly parallel to large-scale tracer contours whereas only their components that are perpendicular to the contours are significant for tracer distribution. We, therefore, introduce here the “effective eddy-induced velocity” or effective eddy-induced velocity (EEIV). It is conceptually analogous to the “effective diffusivity” (e.g., Nakamura, 1996) since the latter is also applied on the direction perpendicular to the tracer contours. We will later demonstrate that this scalar formulation has several advantages over using the vector  $\chi$ . Similarly, we can also define the effective large-scale velocity (ELSV) as will be discussed later.

Equation 13 then becomes

$$\hat{D}_e(\kappa, \chi_\perp; c_L) = \kappa h_L \nabla_c^2 c_L - \chi_\perp |h_L \nabla_c c_L| \delta_c, \quad (14)$$

where the EEIV  $\chi_\perp = \chi \cdot \mathbf{n} \delta_c$ ,  $\mathbf{n}$  is the unit vector along the tracer gradient  $\mathbf{n} = h_L \nabla_c c_L / |h_L \nabla_c c_L|$ , and  $\delta_c$  is a sign function depending on the direction of the zonal-mean meridional tracer gradient:

$$\delta_c = \begin{cases} 1, & \overline{h_L \partial_y c_L}^x > 0 \\ -1, & \overline{h_L \partial_y c_L}^x < 0. \end{cases} \quad (15)$$

The sign function is introduced to simplify interpretation of the scalar  $\chi_\perp$  and eliminate its dependence on the direction of the large-scale tracer gradient. For example, a northward EIV  $\chi$  has a positive projection ( $\chi \cdot \mathbf{n} > 0$ ) onto a front with northward tracer gradient ( $\delta_c = 1$ ) but a negative projection onto a southward gradient ( $\delta_c = -1$ ). By multiplying by  $\delta_c$ ,  $\chi_\perp$  becomes positive in both cases and can be interpreted as the speed at which

eddies displace tracer contours. Its positive (negative) sign implies a northward (southward) advection of the contours by  $\chi$ .

In this study, we use EEIV  $\chi_{\perp}$  to describe and parameterize the eddy-driven frontogenesis. The approach is based on our understanding that the frontogenesis is fundamentally an advective process (McWilliams, 2021), and that the sharp gradient of the front is associated with cross-front transport barrier and suppressed net cross-barrier exchange due to mutual compensation between the large-scale and eddy-induced advectons (Dritschel & McIntyre, 2008).

There are practical advantages of using the advective formulation compared to the purely diffusive one. For example, a complete transport barrier can be guaranteed by requiring a cancellation between cross-frontal components of eddy and large-scale velocities in a coarse-resolution model. Although, gradient sharpening can also be achieved by upgradient diffusion with negative diffusivity, this approach causes numerical instability in models (Lu et al., 2022; Trias et al., 2020). A spatially varying positive diffusivity has an advective effect on tracers through  $\nabla\kappa$  and can potentially lead to frontogenesis, but these effects are already included in the generalized EIV  $\chi$ . Furthermore, Lu et al. (2022) demonstrated that this component ( $\nabla\kappa$ ) of  $\chi$ -vector tends to be smaller than the total  $\chi$ .

Based on the above arguments, we will explore a hypothesis that the eddy-driven frontogenesis can be most effectively modeled by EEIV and that the diffusion  $\kappa$  has a secondary importance. To make progress toward finding a closure for  $\chi_{\perp}$ , we then make further simplification and set the diffusivity  $\kappa$  as a domain and time constant. Using constant diffusivity has been a popular and practical choice in modern ocean climate models (e.g., Meijers, 2014). We selected a constant value of  $\kappa = 80 \text{ m}^2 \text{ s}^{-1}$ , corresponding to the time- and domain-mean value of the diagnosed  $\kappa$  in the upper layer (see Appendix C for details). We confirmed that the frontal width is not sensitive to the exact value of diffusivity, provided it remains relatively small but nonzero, which is necessary for numerical stability. Note that  $\kappa$  is separate from the subgrid tracer diffusivity  $\kappa_r$  in Equation 5 which is used only for numerical stability, along with our new formulation of mesoscale eddy effects.

The unknown,  $\chi_{\perp}$ , is calculated exactly by inverting Equation 14 with the diagnosed  $D_e$  on the left-hand side and  $c_L$  being the tracer solution of the FULL\_EF simulation. For comparison, the vector EIV  $\chi$  is calculated by inverting Equation 13 using two tracers (two equations). More details of the inversion can be found in Haigh et al. (2020) and Lu et al. (2022).

There are several advantages of the scalar formulation (Equation 14) over the vector formulation (Equation 13). First, the frontogenesis can be more readily enforced in the scalar formulation, because it is the EEIV that pushes contours together. The second benefit is the reduction of tracer dependence. The tracer dependence refers to the sensitivity of EEIV  $\chi_{\perp}$  or EIV  $\chi$  to the initial tracer distributions and has been reported before for eddy diffusivity and eddy transport tensor (S. Bachman et al., 2015; Haigh et al., 2020; Kamenkovich et al., 2021; Lu et al., 2022; Sun et al., 2021). In theory, the eddy diffusivity and the (E)EIV are assumed to be quantities inherent to the eddy flow and independent of the tracer. The tracer dependence, thus, contradicts this fundamental assumption and implies a potential bias in representing eddy effects using these quantities. For example, Lu et al. (2022) showed that  $\chi$  is less tracer dependent than the eddy diffusivity, which is interpreted as advantage of the advective formulation. Here we quantify the tracer dependence in the same way as Lu et al. (2022). We first calculate an ensemble of  $\chi_{\perp}$  ( $\chi$ ) from a set of tracers (tracer pairs). The tracer dependence is then defined as the ratio of the ensemble standard deviation to the absolute ensemble mean of  $\chi_{\perp}$  ( $\chi$ ). Figure 6 compares the ratios for  $\chi_{\perp}$  and  $\chi$ . We see that the tracer dependence of  $\chi_{\perp}$  is significantly reduced compared to that of  $\chi$ , although it is still larger than 100%. Our additional analysis further shows that the sign function  $\delta_c$  is important for the reduction in tracer sensitivity. These results demonstrate the benefits of using the EEIV to represent eddy effects.

In the simulations described in the next section, we use the net tracer conservation of Lu et al. (2022) to guarantee that the EEIV formulation (Equation 14) does not introduce sources and sinks in the global tracer inventory. A correction is added to the parameterized eddy forcing  $\hat{D}_e$ , that makes its global integral zero in the closed domain. The correction is conceptually similar to the conservation enforcement used in stochastic parameterizations (Leutbecher et al., 2017). We describe it and confirm the tracer conservation in Appendix D.

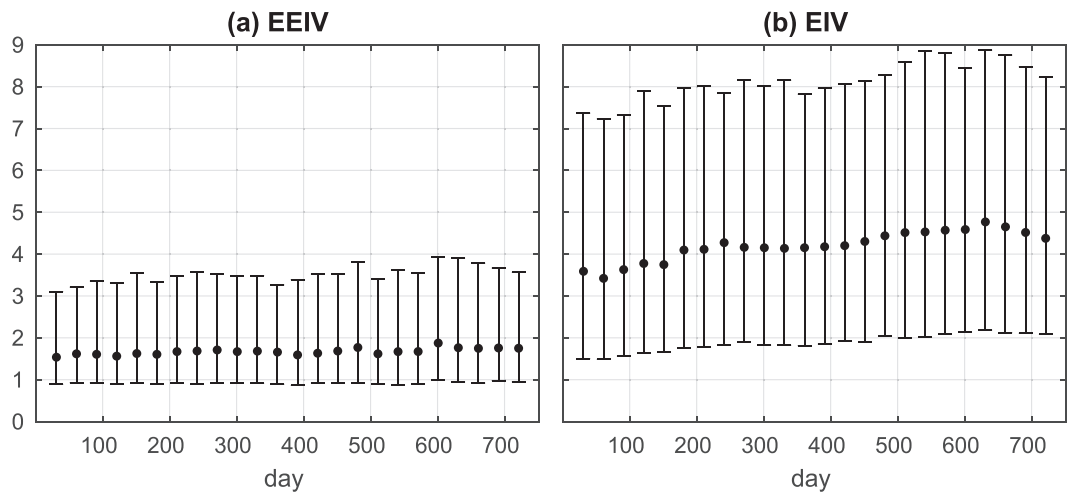


**Figure 6.** Tracer dependence, calculated as a ratio of the standard deviation to the absolute ensemble mean, of (a) effective eddy-induced velocity (EEIV)  $\chi_{\perp}$  and (b) eddy-induced velocities (EIV)  $\chi$ . Error bars denote the median and the 25–75th percentile range of the ratio. The ensemble of EEIV includes 10 estimates diagnosed from 10 (passive temperature tracer, chemical tracer and eight idealized tracers) tracers. The ensemble of EIV includes 10 estimates randomly chosen from all the 45 estimates (45 tracer pairs generated from 10 tracers). For EIV, the ratios of its two horizontal components are averaged. Results are for the upper layer.

#### 4. Effect of Eddies on the Front

In this section, we explore the role of eddies in the front formation by analyzing the frontogenesis equation and examine its physical mechanism using the concept of EEIV. We mainly show the results for the passive temperature tracer but confirmed that all conclusions remain the same for the chemical tracer as well.

##### 4.1. Analysis of the Frontogenesis Equation

To examine how eddies interact with the large-scale flow in sharpening the front, we study the frontogenesis Equation 12 for the FULL\_EF experiment. Figure 7a shows the time series of all terms in the budget averaged within the jet region. The tendency term fluctuates around zero after the tracer has been stirred up, showing that a statistically steady state of tracer is reached. Several important points are drawn from the budget. First, the area-averaged eddy term  $E$  remains positive, meaning that it acts to increase the magnitude of the tracer gradient. This implies that eddies are sharpening the front, which agrees with the previous comparison between the NO\_EF and FULL\_EF simulations. In contrast, the effect of the large-scale current, characterized by the negative  $L$  term with similar magnitude with  $E$ , is to weaken the gradient and broaden the front. There is a large inverse spatial correlation of  $-0.9$  between  $L$  and  $E$ , confirming the tendency of the large-scale and eddy currents to balance each other in the front evolution. The residual from the sum of  $E$  and  $L$  is at least one order of magnitude smaller than any of the terms and is balanced by the sum of the (squared) tracer gradient tendency, the diffusion  $A$  and the relaxation  $R$ . Diffusion is small and negative, as expected for it works to smooth the front. The relaxation term has a similarly small magnitude.

Figure 7b further shows that the large-scale velocity confluence term  $L_{con}$  plays a dominant role in the broadening of the front, which may appear counter-intuitive since the large-scale advection brings cold water from the north and warm water from the south. However, as is demonstrated by the experiment NO\_EF, this action by large-scale flow induces a much broader front than FULL\_EF, which opposes the frontal sharpening by eddies (Figure 5).

The nearly steady state of the FULL\_EF simulation in the frontal region results from a balance between the frontal sharpening induced by eddies and the frontal broadening induced by large-scale advection. The latter effect can be interpreted as the tendency of the large-scale current to create a broader front, as in the NO\_EF simulation. The role of eddies in maintaining a sharp front aligns with earlier studies, highlighting their importance in sustaining PV fronts in the western boundary current extensions (Berloff, 2005b; Shevchenko & Berloff, 2015; Waterman & Jayne, 2011).

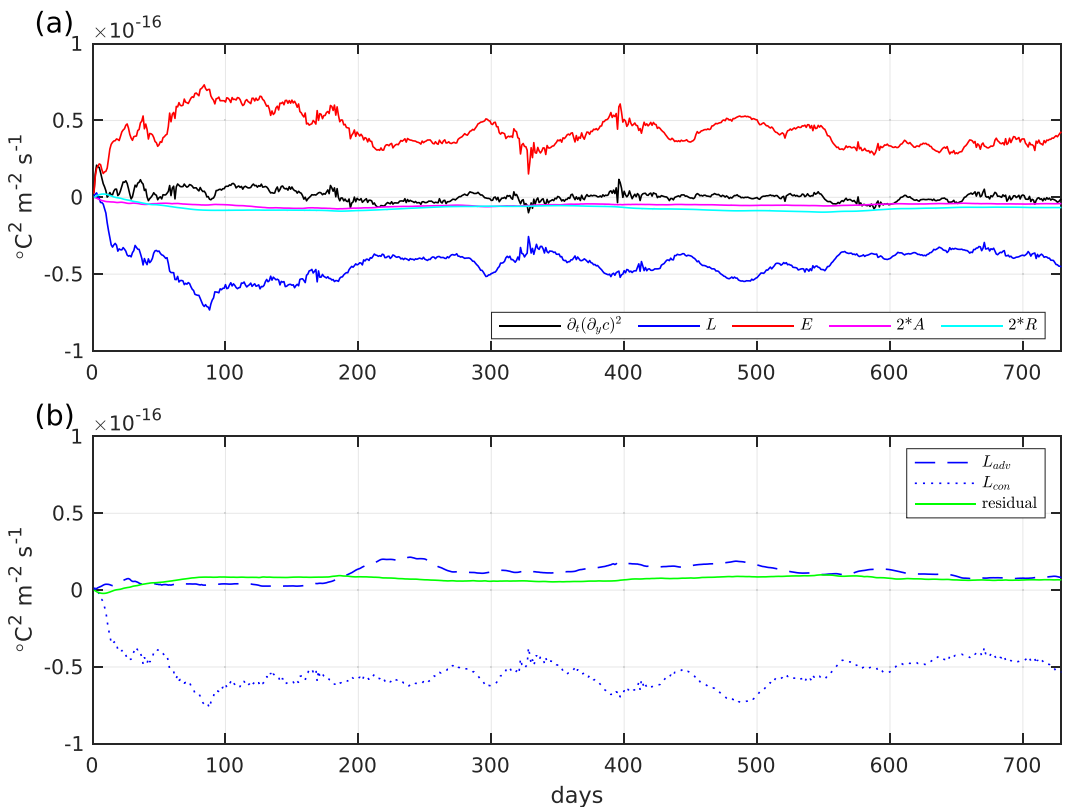


**Figure 7.** Time series of terms in the frontogenesis Equation 12 averaged in the jet region (defined in Figure 5). (a) The tendency, the effect of large-scale advection current  $L$ , the effect of eddies  $E$ , the effect of subgrid diffusion  $A$  and the effect relaxations  $R$  terms.  $A$  and  $R$  are multiplied by a factor of 2 for presentation. (b) The two components of  $L$ :  $L_{adv}$  and  $L_{con}$ , and the residual of the entire budget. Results are for the passive temperature tracer in the upper layer.

To further explore the relationship between large-scale and eddy influence on the front, we compute the pointwise time correlations between the frontogenetic budget terms (Figure 8). We observe that large negative correlations between  $L$  and  $E$  are concentrated along the jet, indicating strong mutual compensation between the large-scale and mesoscale processes in this region, where eddy forcing is particularly strong (Figures 4a and 4b). The tendency term in the jet region is small and not significantly correlated to either  $L$  or  $E$  (Figures 8a and 8c), which further outlines the balance between the large-scale confluence and an opposite effect of eddies, which will be further explored using the EEIV  $\chi_\perp$  in the following section.

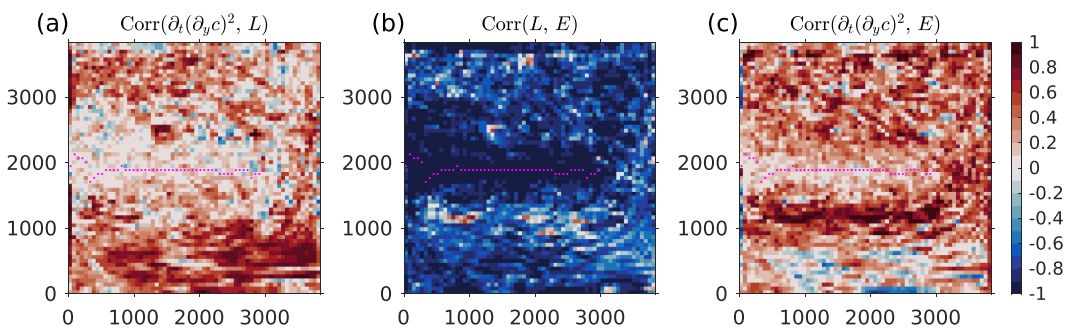


**Figure 8.** Pointwise correlations between different terms in the frontogenesis Equation 12 over 2 years in the upper layer: (a) between the tendency and large-scale flow effect on the front  $L$ ; (b) between the large-scale flow  $L$  and eddy effects  $E$  and (c) between the tendency and the eddy effect  $E$ . Magenta dots are the jet core.

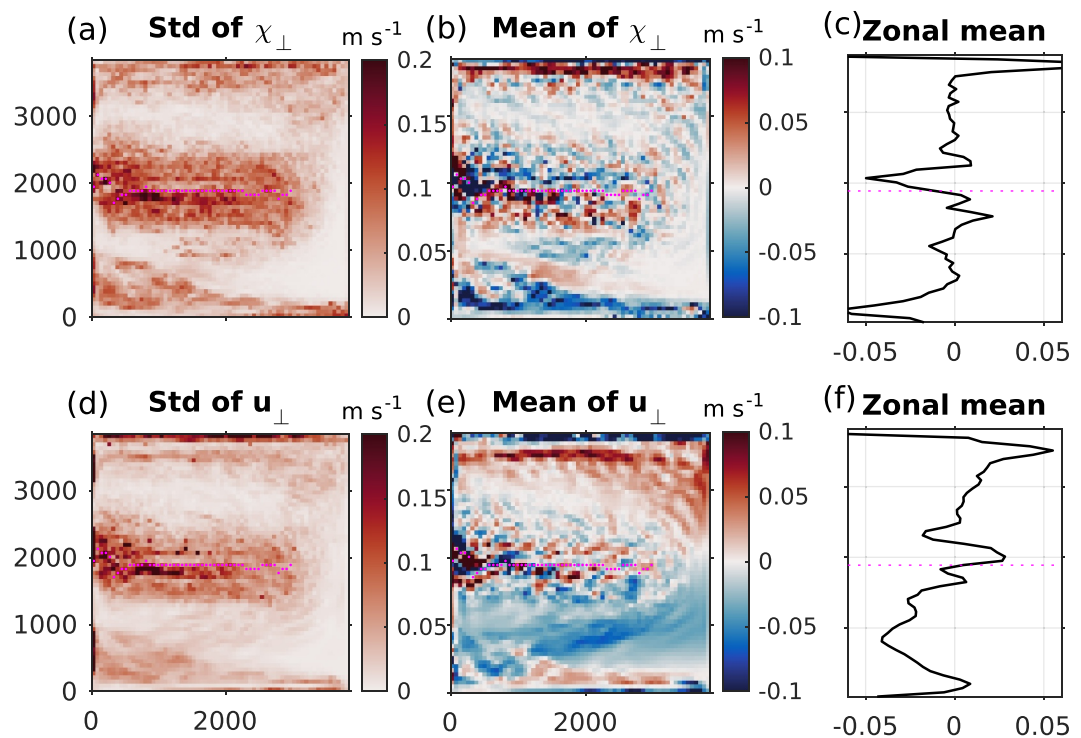


**Figure 9.** (a) The standard deviation, (b) time mean and (c) time- and zonal-mean of the effective eddy-induced velocity  $\chi_{\perp}$ . (d)–(f) Same but for the effective large-scale velocity  $u_{\perp}$ . Both are projected onto the passive temperature tracer. The data are for years 21–22. Magenta dots in color plots are the jet core. Magenta dotted line in (c) and (f) shows the zonal-mean latitude of the jet core. Outliers in  $\chi_{\perp}$  that fall outside the 1%–99% percentile are excluded for presentation purposes.

Outside of the jet region, the tendency is more strongly correlated to  $E$  than  $L$ , which is likely due to the transient eddy effect on tracer contours. However, since tracer concentrations in that area show no significant differences between the NO\_EF and FULL\_EF simulations, and our main focus is on the frontal region, we do not examine the effect of eddies outside the jet region.

#### 4.2. Importance of the Eddy-Induced Advection

Our results have so far demonstrated that mesoscale eddies sharpen the front while the large-scale flow plays an opposite role. We now use the eddy-induced advection to explain the underlying physical mechanism of the eddy-driven frontal sharpening and the compensation between eddies and large-scale currents. Note that the same analysis would be considerably more complex if a purely diffusive framework were used to describe the eddy effects. This is because, mathematically, exact compensation between large-scale advective fluxes  $\mathbf{u}_L c_L$  and diffusive fluxes  $\kappa \nabla_c c_L$  cannot be achieved for an arbitrary tracer.

Figure 9 shows the standard deviation, time-mean and zonal-mean of the EEIV  $\chi_{\perp}$ , as well as the ELSV  $u_{\perp} = \mathbf{u}_L \cdot \mathbf{n} \delta_c$  for the passive temperature tracer. In general,  $\chi_{\perp}$  and  $u_{\perp}$  are of the same order of magnitude, once again demonstrating their equally important roles in tracer distributions. The standard deviation of  $\chi_{\perp}$  exceeds its time mean and concentrates along the jet, indicating a large time variability as the eddy forcing. The time-mean  $\chi_{\perp}$  is mostly negative (positive) at the north (south) of the jet core, which means southward (northward) advection of tracer contours (Figures 9b and 9c). It means that eddies on both sides of the jet advect cold and warm water toward each other, squeezing the temperature contours, and thus sharpening the front. The eddy-induced squeezing of tracer contours has been reported by several studies in terms of up-gradient eddy-induced diffusion (Haigh & Berloff, 2021; Haigh et al., 2021b; Kamenkovich et al., 2021). Here, it is effectively described by the eddy-induced advection with a clear spatial structure reflecting the physical mechanism of the eddy-driven frontogenesis. The ELSV  $u_{\perp}$  has an opposite profile to  $\chi_{\perp}$  in the jet region (Figure 9f), confirming the compensation between the two as discussed above. Also note that the EEIV at the southern flank of the GS core is

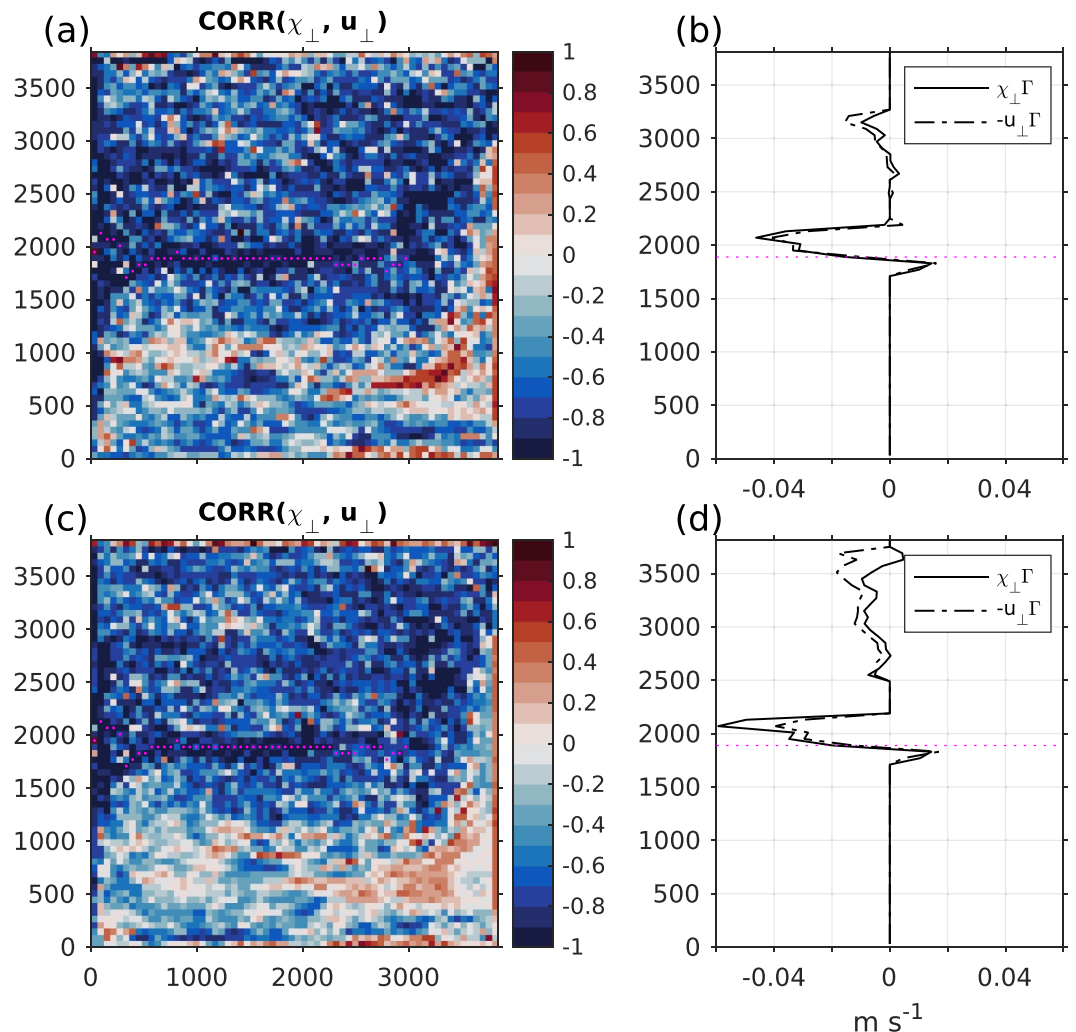


**Figure 10.** (a) Correlation between  $\chi_{\perp}$  and  $u_{\perp}$  diagnosed for the passive temperature tracer. (b) Meridional profiles of the time- and zonal-mean  $\chi_{\perp}\Gamma$  (solid) and  $-u_{\perp}\Gamma$  (dash), in which  $\Gamma$  (defined by 17) ensures that only points with sufficiently large (80th percentile and above) tracer gradient norms are considered. (c)–(d) Same as (a)–(b), respectively, but for the chemical tracer. Magenta dots are the jet core. All fields span over 2 years and are in the upper layer.

much smaller than that at the northern flank. This difference could explain why the tracer difference between NO\_EF and FULL\_EF is more pronounced to the north of the GS (Figure 5f).

To further demonstrate a close relation between  $\chi_{\perp}$  and  $u_{\perp}$ , Figures 10a and 10c show significant negative correlations between these two variables in the jet region, for both the passive temperature and chemical tracers. This is also consistent with the negative correlation between the large-scale and eddy terms in the frontogenesis equation (Figure 8b). The relationship will be further used to derive a functional form of EEIV in terms of ELSV in the next section.

## 5. Simulation of the Front in the Coarse-Resolution Tracer Model

The goal of this section is to examine the importance of EEIV in numerical simulations, in which the eddy forcing is replaced by  $D = \hat{D}_e(\chi_{\perp}; c)$  in Equation 6. As we have seen in the previous section, ELSV acts to broaden the front, while the EEIV sharpens it. In this section we will see that the front quickly dissipates unless this relationship between EEIV and the front is enforced. In particular, a simple functional form of EEIV that enforces such relationship is demonstrated to effectively sharpen the front. This exercise paves a way toward a full parameterization, which is reserved for a future study with a coarse-resolution dynamical model.

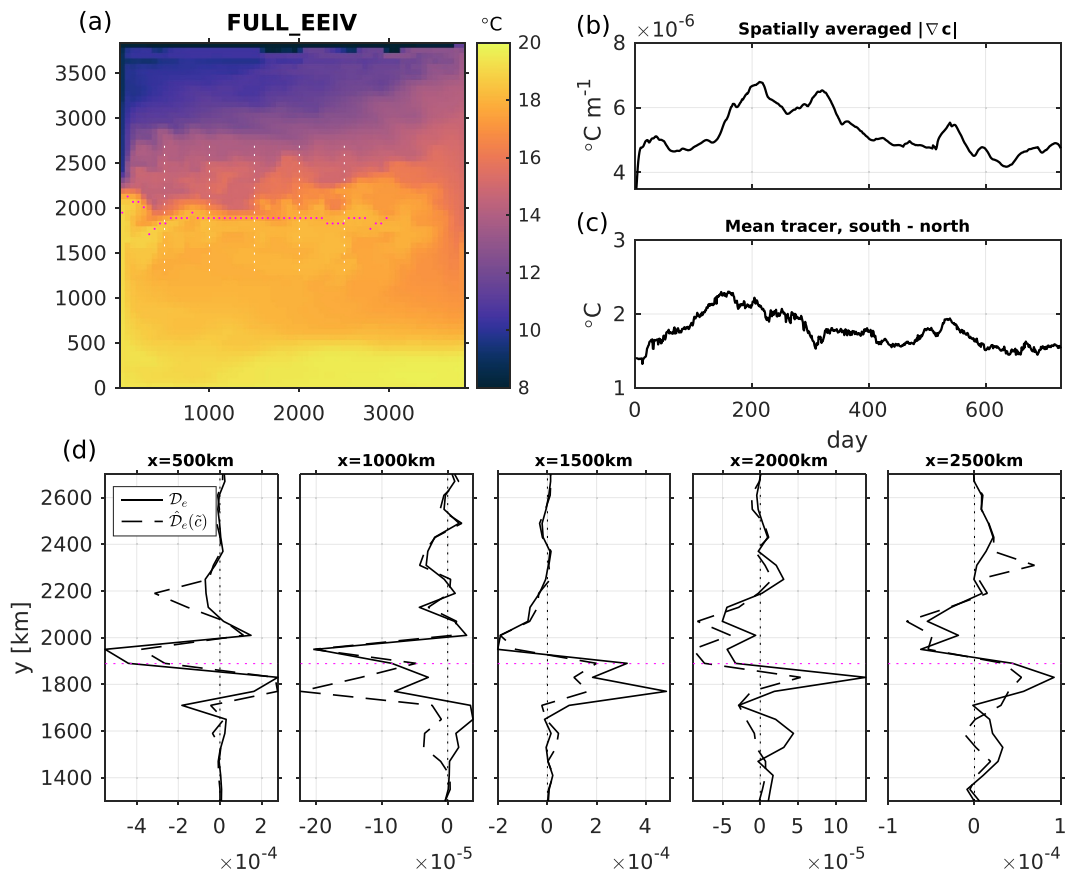


**Figure 11.** Passive temperature solution in the FULL\_EEIV simulation. (a) Snapshot at day 361 years 21. (b)–(c) The spatial averaged tracer gradient norm and the tracer difference between the south and north of the jet, respectively, as functions of time (same as in Figures 5d and 5e). (d) Meridional profiles of the time-averaged (over year 21–22) true eddy forcing  $D_e$  and parameterized eddy forcing  $\hat{D}_e(\chi_{\perp}; c_L)$  [ $^{\circ}\text{C m s}^{-1}$ ] diagnosed in the FULL\_EEIV run, at different longitudes shown by the white dots in (a). Magenta dots in (a) and (d) denote the jet core.

### 5.1. Diagnosed Full EEIV

Our first step is to apply the full EEIV  $\chi_{\perp}$ , diagnosed directly from the full tracer simulation, in the coarse-resolution tracer model. We denote this experiment as FULL\_EEIV. The full  $\chi_{\perp}(\mathbf{x}, t)$  is calculated by inverting Equation 14 at each time and location for the passive temperature tracer, with the diagnosed eddy forcing  $D_e$  on the left hand side and reference tracer  $c_L$  on the right. Using the full EEIV, however, acts to diffuse the front instead of sharpening it (Figure 11). Compared to FULL\_EF, the tracer has a large bias near the jet core, and the front becomes even weaker than in the NO\_EF simulation (Figures 5e, 5f, 11b, and 11c). This shows a dramatic loss of the frontogenesis skill of the full  $\chi_{\perp}$  in the jet region. In the rest of the domain the solution in FULL\_EEIV is visually indistinguishable from FULL\_EF.

The failure of the full  $\chi_{\perp}$  to sharpen the front, instead causing it to weaken, is due to the deterioration of the spatiotemporal covariability between the front position and eddy forcing. For effective frontogenesis, the time- and space-dependent eddy forcing  $D_e$  and EEIV  $\chi_{\perp}$  (Figures 4b, 4c, 9a, and 9b) must both stay closely correlated with the meandering front. Retaining this covariability between the forcing and the front in space and time is a nearly impossible task because even a small error in the runtime solution  $c$  leads to an error in the predicted eddy forcing  $\hat{D}_e(\chi_{\perp}; c)$ . These errors arise due to numerical factors, including insufficiently frequent time sampling of  $\chi_{\perp}$  relative to the model's internal time step, as well as inaccuracies in the inversion of large matrices when solving Equation 14. The initially small errors can then grow rapidly due to chaotic sensitivity. For example, a bias in the eddy forcing can cause cooling in places where warming is needed for sharpening the front, which in turn

amplifies errors in the solution. A similar property is described in Section 3.1, where we used the full space- and time-dependent eddy forcing in the same model.

In support of these conclusions, Figure 11d compares several meridional sections of the time averaged  $\hat{D}_e(\chi_{\perp}; c)$  and original full  $D_e$ .  $\hat{D}_e$  differs more from  $D_e$  around the front ( $1,600 \text{ km} < y < 2,400 \text{ km}$ ) than in other regions, resulting in a significantly weaker front despite having the “exact”  $\chi_{\perp}$ . In the following section, we show that the frontogenesis can be readily enforced when the relationship between the large-scale (zonal-mean) ELSV and EEIV is explicit, further demonstrating the advective nature of eddy effects and the utility of the advective approach in representing the eddy-driven frontogenesis.

## 5.2. Functional Form of EEIV

In the previous section, we observed that the full time- and space-dependent EEIV  $\chi_{\perp}$  cannot guarantee frontogenesis and instead aggravates biases in the simulation. We hypothesized that the correlation between  $\chi_{\perp}$  and  $u_{\perp}$  is the key factor for the frontogenesis, and when such relation is lost the front is destroyed. In this section, we confirm this hypothesis by demonstrating that a simple functional form of  $\chi_{\perp}$  capturing the essential relation between EEIV and ELSV results in frontogenesis. This result will demonstrate that the eddy-driven compensation of the large-scale advection is essential for creating a sharper front. Although the simplicity of the relationship hints at a potential closure, the development of a practical parameterization is deferred to a future study.

Guided by the close relationship between EEIV and ELSV (Figures 10a and 10c), we propose a simple functional form for  $\chi_{\perp}$  in terms of the large-scale field  $u_{\perp} = \mathbf{u}_L \cdot \mathbf{n}\delta_c$ :

$$\hat{\chi}_{\perp} = -\alpha u_{\perp} \Gamma, \quad (16)$$

where the coefficient  $\alpha$  quantifies the efficiency of the partial compensation between the eddy and large-scale advections. A function  $\Gamma$  is used to eliminate points where the tracer is well mixed and the frontogenesis is not expected:

$$\Gamma = \begin{cases} 1, & |\nabla c| \geq |\nabla c|_{thres} \\ 0, & |\nabla c| < |\nabla c|_{thres} \end{cases} \quad (17)$$

Here the threshold  $|\nabla c|_{thres}$  is chosen as the 80th percentile of the tracer gradient norms across the upper layer. This corresponds to  $4 \times 10^{-6} \text{ }^{\circ}\text{C} \cdot \text{m}^{-1}$  for the passive temperature and  $8 \times 10^{-7} \text{ mol} \cdot \text{km}^{-3} \cdot \text{m}^{-1}$  for the chemical tracer. Note that the functional form (Equation 16) is in principle analogous to the amplification of the eddy backscatter (e.g., Berloff, 2018; Jansen et al., 2019).

Figures 10b and 10d compare the time and zonally averaged profiles of  $\chi_{\perp}\Gamma$  and  $-u_{\perp}\Gamma$  diagnosed for the passive temperature and idealized chemical tracers. We see that the two profiles closely resemble each other for each of these tracers.  $\chi_{\perp}$  rapidly grows in the meridional direction from zero at the jet core to a large negative (positive) value in the north (south) and then decays further away from the core. This “dipole” structure is consistent with our previous discussion of the eddy-driven confluence, that acts to advect (squeeze) tracer contours from both sides toward the jet core whereas the large-scale flow counteracts this effect. Importantly, the profiles of  $\chi_{\perp}$  for the two different tracers are very similar. This is another manifestation of the reduced tracer dependence in  $\chi_{\perp}$  as discussed in Section 3.3.

We next apply the relation (Equation 16) to the coarse-grid tracer model in order to demonstrate the frontogenetic effect of eddy-induced advection. The full eddy forcing we use is (inserting Equations 14–16):

$$\hat{D}_e(\kappa, \alpha) = \kappa h_L \nabla_c^2 c_L + \overline{\alpha u_{\perp} |h_L \nabla_c c_L| \delta_c \Gamma}, \quad (18)$$

where the overbar is a zonal average. The zonal average is applied to reduce mesoscale variability in the eddy forcing and can be replaced by streamwise averaging or smoothing in more realistic applications. The along-front mesoscale variations are shown to lead to local decorrelations between  $\hat{\chi}_{\perp}$  and the front position, which can cause growth of errors (see previous sections).

The remaining step is to specify the nondimensional parameter  $\alpha$ , which can be expected to depend on the flow properties and model resolution. The pointwise regression of  $\chi_{\perp}$  on  $u_{\perp}$  indeed reveals a complex spatial distribution (not shown), which has values from 0.6 to 1.2 in the jet region and suggests a varying degree of compensation between EEIV and ELSV. It is unclear whether the spatial variability in  $\alpha$  significantly affects the simulation, but deriving a functional (space- and time-dependent) form for  $\alpha$  is a challenging exercise that falls beyond the scope of this study. Instead, we take  $\alpha$  to be a constant, and explore sensitivity of the frontal width to this parameter. In practical applications,  $\alpha$  can be set to a value that achieves a desired front width, if such width is known, for example, from observations. This “tuning” is a common practice in ocean modeling, particularly when selecting critical physical parameters such as neutral and GM diffusivities. (e.g., Eden, 2006; Grooms & Kleiber, 2019; Holmes et al., 2022; Meijers, 2014). In our study, we can compare the results to FULL\_EF, which serves as our ground truth, as the front in this simulation can be considered the best achievable at this resolution. In what follows, we will observe, however, that the sensitivity to  $\alpha$  is rather modest, and the tracer front is sharpened as long as  $\alpha$  is greater than zero.

We performed a series of numerical experiments with the values of  $\alpha$  ranging from 0.1 to 1.0. We found that the sharpness of the front increases with  $\alpha$ . This is expected because  $\alpha$  controls the magnitude of EEIV and tracer eddy forcing, thus directly affecting the front sharpness. Of all considered values,  $\alpha = 0.4$  gives the most accurate front for our model, and we only show the corresponding solution here (denoted as “FUN\_EEIV”). Figure 5 shows the passive temperature tracer and the gradient from the FUN\_EEIV experiment in comparison to those from NO\_EF and FULL\_EF. We see that the sharp front, as characterized by both the temperature difference and the gradient norm in the jet region, is well reproduced here after the first 200 days (Figures 5d and 5e). The meridional profiles (Figure 5f) further show that the meridional gradients across the jet are sharpened and are close to their values in FULL\_EF.

Simulations of the chemical tracer lead to similar results (Figure 12). The front is about 30% sharper in FULL\_EF compared to NO\_EF (Figure 12e). This eddy-driven frontogenesis is well reproduced in the FUN\_EEIV run with the same of the parameter  $\alpha$  as for the passive temperature tracer:  $\alpha = 0.4$ . This demonstrates the robustness of our conclusions despite tracer dependence (Section 4.2).

## 6. Conclusions and Discussion

This study examines the importance of mesoscale eddies in the formation and evolution of large-scale oceanic tracer fronts, using the fronts along the eastward jet extensions of western boundary currents in an idealized double-gyre system as an example. The focus is on the eddy-induced stirring of tracers, while the contributions of eddies to momentum and mass/density fluxes are beyond the scope. Our main conclusion is that eddy stirring sharpens the front, counteracting the large-scale flow's tendency to broaden it. The study quantifies these effects using the concept of generalized eddy-induced advection, highlighting their advective nature. The demonstrated efficiency of EEIV in front sharpening paves the way for future development of effective parameterizations in coarse-resolution models. The simple functional form of EEIV considered in this study is a first step in that direction.

The analysis of eddy effects is based on eddy forcing, which encompasses all eddy-related terms in the tracer budget, making it ideal for situations where most of these terms influence tracer evolution. If such eddy forcing is accurately captured in coarse-resolution simulations, the tracer field is likely to be simulated accurately as well. The key result is that the eddy forcing acts to sharpen the large-scale tracer front, as demonstrated by both the sensitivity tracer experiments in an offline tracer model and the analysis of the frontogenesis equation. In particular, the front is significantly sharper in the simulation with eddy forcing compared to the run without, even though the total mass flux, which is the sum of large-scale and eddy-driven mass fluxes, is the same in both simulations. The analysis of the frontogenesis equation further shows that the eddy-driven frontogenesis is balanced by the effects of the large-scale flow. Specifically, the large-scale currents act to induce a broader tracer front primarily via the confluence (strain) of the large-scale velocity.

The frontal sharpening by eddies and its partial compensation by the large-scale advection is conveniently quantified using a recently proposed generalized advective framework (Lu et al., 2022). In this study, we further modify this approach by using an EEIV, which is a speed at which eddies advect large-scale tracer contours. The EEIV effectively describes the physical mechanism of the eddy-driven frontogenesis: taking the passive temperature as an example, the eddies facilitate the advection of warmer (colder) water to the warm (cold) side of the

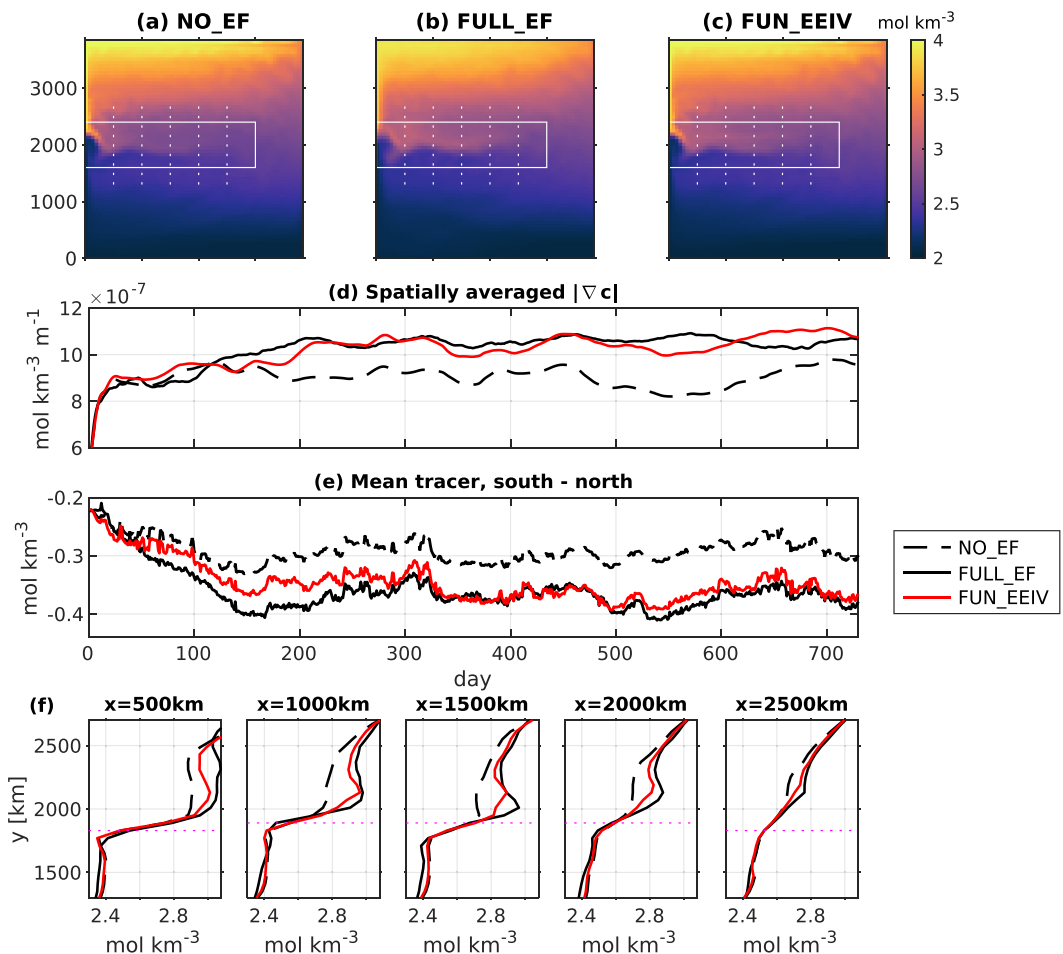


**Figure 12.** Tracer solutions and front magnitudes in different experiments for the chemical tracer. The legends and meaning of each subplot are the same as Figure 5.

front, squeeze the tracer contours together, and thus sharpen the front. This process can be interpreted as eddy-driven confluence and would be challenging to describe by the eddy diffusion alone. For example, recent studies (Haigh & Berloff, 2021; Haigh et al., 2021b; Kamenkovich et al., 2021) have found persistent pairs of positive and negative eigenvalues of the eddy diffusivity tensor (“polarity”) that can lead to stretching of the tracer contours and producing tracer filaments or fronts (Haigh & Berloff, 2022). Although the above polarity in the diffusion tensor can result in frontogenesis, negative diffusivities are numerically unstable, and the above reported compensation with the large-scale advection is hard to enforce for an arbitrary tracer using the diffusive model.

The EEIV formulation has two main advantages over the originally proposed vector formulation of the eddy-induced velocity (EIV,  $\chi$  (Lu et al., 2022)). The first advantage is the reduced tracer dependence, which means weaker sensitivity of  $\chi_{\perp}$  to initial tracer profiles and thus smaller bias in simulating different tracers. It indicates that the scalar EEIV is determined by the flow to a larger degree than is the vector EIV. Since Lu et al. (2022) also shows a reduced tracer dependence of  $\chi$  compared to the eddy diffusivity, the EEIV  $\chi_{\perp}$  is also superior to the diffusivity in this regard. The second advantage is that the uncovered eddy-induced frontal sharpening can be more readily enforced in coarse-resolution models by specifying  $\chi_{\perp}$  rather than the vector  $\chi$ . The EIV framework is much less practical because the vector  $\chi$  is nearly parallel to the tracer contours in the frontal region and only a small cross-contour (EEIV) component of  $\chi$  matters for tracer evolution. This subtle effect is challenging to simulate and even small errors in  $\chi$  may yield large biases in the frontal structure.

To account for the partial compensation between eddy-driven and large-scale advection in the frontal region, we considered a functional form of EEIV in terms of the ELSV. The functional expression captures the partial balance between EEIV and ELSV in the frontal region: the EEIV sharpens the front while the ELSV acts to broaden it. This effectively reproduces the eddy-driven frontogenesis in the tracer simulation on a coarse grid. The parameter in the resulting closure is taken to be constant for simplicity. Despite this simplification, the constant value — determined through “tuning” — was sufficient to produce a realistic front, highlighting the efficiency of the advection-based approach.

The results in this study demonstrate the effectiveness of the advective framework for representing such important effects of eddies as frontogenesis and filamentation. Nevertheless, the simple functional form considered here does not constitute a complete parameterization because the large-scale flow and stratification are both derived from the eddy-resolving solution. Although the flow and stratification are projected onto the coarse grid whose spatial resolution falls in the intermediate-resolution range, they are not directly simulated at that resolution. In fact, the resolution in such models is sufficient to detect the tracer front but remains too coarse to accurately simulate its dynamics. The advantage of using this approach is that it allows us to focus on the role of tracer eddy forcing without the ambiguity from biases in momentum and mass fluxes. However, further work is needed to implement the advective method in models that do not fully resolve mesoscale processes.

The new approach in this study has, nevertheless, potential to evolve into an effective parameterization. In general, accurately simulating the ocean state requires representing the effects of eddies on momentum, density, and tracers. For example, the eddy-driven “backscatter” scheme has been successfully used to energize partially resolved mesoscale eddies and improve the simulation of ocean currents in eddy-permitting models (S. Bachman, 2019; Berloff, 2018; Grooms et al., 2015; Jansen & Held, 2014; Jansen et al., 2019; Yankovsky et al., 2024; Zanna et al., 2017). Notably, Yankovsky et al. (2024) recently showed that a backscatter-only model could adequately push the eddy-permitting model toward the eddy-resolving regime even without turning on the GM scheme. Our study demonstrates, however, that having even the perfect mass (density) fluxes (or ocean current) is not sufficient for the simulation of a sharp tracer fronts. The missing part is the eddy tracer stirring that comes from the correlation between the mesoscale velocity and tracer anomalies, which turns out to be critical for the front formation. It also remains to be seen if these stirring and resulting eddy-driven frontogenesis and potential formation of the transport barriers can be accurately recovered by energizing under-resolved eddies through the backscatter. The proposed advective framework can then effectively augment these parameterizations of eddy momentum and density transfer and be used to enforce frontogenesis. The advective approach is particularly appealing in this regard because it complements the existing GM parameterization in the tracer equation by incorporating a correction for frontogenesis and other advective effects of eddies.

An interesting finding of this study is that the EEIV with full spatiotemporal variability fails to guarantee the frontogenesis and instead leads to further deterioration of the front from the simulation without eddy forcing. This is due to the rapid loss of correlation between the meandering front and eddy forcing, which leads to chaotic sensitivity of the frontal evolution to the eddy forcing. In contrast, a simple functional form of the eddy forcing is significantly more successful because it is designed to reproduce the most important properties of the eddy effects. In this study, such properties involve squeezing of the tracer contours from the north and south of the jet. However, identification of such essential features may not be always straightforward and would require careful analysis of what properties (e.g., spatiotemporal structures) of eddy effects are most important for the specific ocean phenomenon of interest. Machine learning approaches can be particularly promising in this regard since they can extract essential properties from complex fields and even discover new physical relations (Guillaumin & Zanna, 2021; Partee et al., 2022; Perezhogin et al., 2023; Ross et al., 2023; Zanna & Bolton, 2020).

This study focuses on the significance of mesoscale eddies on the large-scale tracer front. Submesoscale currents, another key component of oceanic flows that are missing in this study, can also contribute to the frontogenesis (McWilliams, 2016). These three-dimensional currents usually manifest themselves as overturning cells associated with upwelling and downwelling that enhance the fronts in ocean surface. Note that mesoscale eddies can also induce a similar overturning circulation in the surfacemixed layer (Li & Lee, 2017; Li et al., 2016), which could be another mechanism for eddy-induced frontogenesis in the upper ocean. The fronts characterized by vertical motions occurring on horizontal scales of  $O(1\text{--}10 \text{ km})$  and in the mixed layer, however, are absent in our model. Studies of the importance of different scales for large-scale fronts should be continued in more realistic

settings, as they provide insights on frontal dynamics and development of eddy parameterization scheme for non-eddy-resolving ocean models.

## Appendix A: Coarse Graining of the Mass Flux

The first step of defining the large-scale mass flux  $\mathbf{U}_L$  (Equation 9) is to coarse grain the high-resolution mass flux  $\mathbf{U}$ . The coarse graining must preserve the divergence of the mass flux, because it determines the layer thickness. This is achieved here by utilizing the Helmholtz decomposition as follows. The high-resolution mass flux  $\mathbf{U}$  is first decomposed into its divergent and rotational components (Maddison et al., 2015):

$$\mathbf{U} = \nabla\phi + \hat{\mathbf{z}} \times \nabla\psi, \quad (\text{A1})$$

$$\nabla \cdot \mathbf{U} = \nabla^2\phi, \quad (\hat{\mathbf{z}} \times \nabla) \cdot \mathbf{U} = \nabla^2\psi,$$

where  $\phi$  is potential for the divergent component ( $\nabla\phi$ ),  $\psi$  is streamfunction for the rotational component ( $(\hat{\mathbf{z}} \times \nabla)\psi$ ),  $\hat{\mathbf{z}}$  is the unit vector in the vertical direction, and  $(\hat{\mathbf{z}} \times \nabla) \cdot (\dots) = (-\partial_y, \partial_x)$  is the horizontal curl operator.

We then coarse grain (denoted by an angle bracket) the flux divergence to get  $\langle \nabla \cdot \mathbf{U} \rangle$ . To get a corresponding divergent component, we solve the Poisson problem on the coarse grid with zero norm-flux boundary condition

$$\nabla_c^2\phi^c = \langle \nabla \cdot \mathbf{U} \rangle, \quad (\text{A2})$$

where  $\phi_c$  is the potential for the divergent component ( $\nabla_c\phi_c$ ) on the coarse grid. We also coarse grain  $\psi$  to get the streamfunction for the rotational component on the coarse grid

$$\psi_c = \langle \psi \rangle. \quad (\text{A3})$$

The coarse-grained mass flux is then defined as

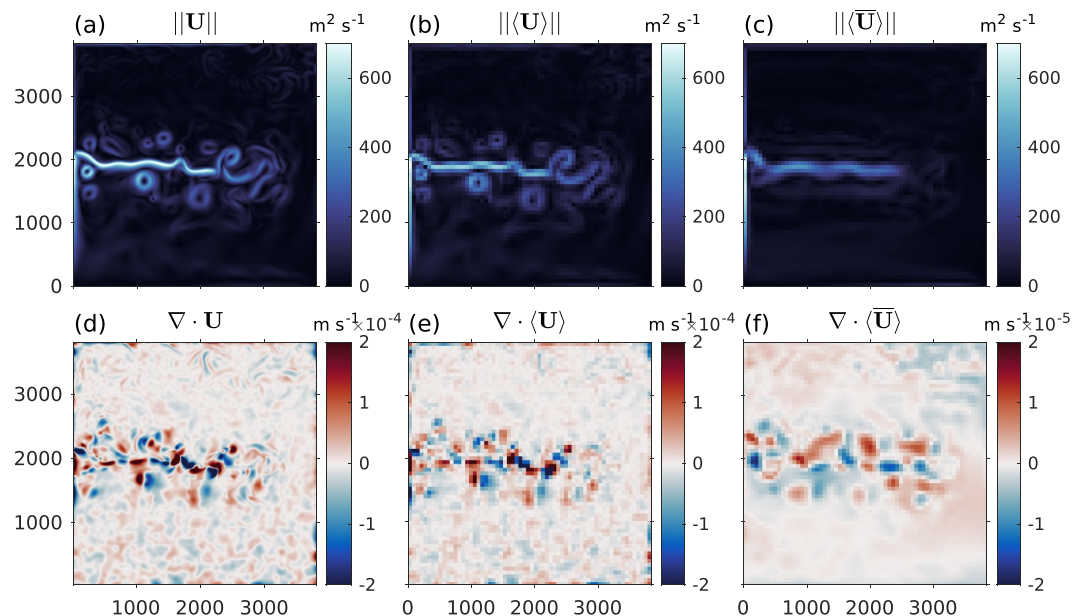


**Figure A1.** Norm of (a) the high-resolution mass flux, (b) the coarse-grained mass flux, and (c) the large-scale mass flux  $\mathbf{U}_L$  (coarse-grained and time filtered), at day 120 years 21 in the upper layer. (d)–(f) Divergences of the mass fluxes in (a)–(c), respectively. Note the color scale in (f) is 10 times smaller than in (d) and (e).

$$\nabla_c \cdot \langle \mathbf{U} \rangle = \nabla_c^2 \phi_c = \langle \nabla \cdot \mathbf{U} \rangle, \quad (\hat{\mathbf{z}} \times \nabla_c) \cdot \langle \mathbf{U} \rangle = \nabla_c^2 \psi_c.$$

Its divergence by definition equals the coarse-grained divergence of the high-resolution mass flux, which guarantees reasonable layer thickness and tracer solutions on the coarse grid. The coarse-grained mass flux also preserves the flow structure in  $\mathbf{U}$ , because the streamfunction for the rotational component of  $\langle \mathbf{U} \rangle$  is directly projected from that of  $\mathbf{U}$ .

For a comparison, we also attempted simple coarse graining of the zonal and meridional components of  $\mathbf{U}$ . However, the resulting mass flux has a exaggerated divergence that is more than 10 times larger than the divergence of  $\mathbf{U}$  and causes instabilities in the coarse-grid continuity and tracer simulation. This issue is due to the non-commutativity between discrete spatial-derivative operators and discrete coarse-graining (Manz & Zanna, 2014). A more rigorous divergence-preserving coarse-graining method can be found in Patching (2022) but is not applied here due to its complexity.

The large-scale mass flux  $\mathbf{U}_L$  is then obtained by time filtering  $\langle \mathbf{U} \rangle$  with a 180-day window. Figure A1 shows its norm and divergence, as well as those of  $\mathbf{U}$  and  $\langle \mathbf{U} \rangle$ . We see that the elongated jet extension is well retained in  $\mathbf{U}_L$  and the divergences of  $\langle \mathbf{U} \rangle$  and  $\mathbf{U}_L$  do not exceed the high-resolution flux divergence. The time filtering eliminate the mesoscale structures (e.g., vortices) in  $\langle \mathbf{U} \rangle$  (Figures A1b and A1c). We conclude that the combination of coarse-graining and time averaging effectively remove the mesoscale variability in the flow.

## Appendix B: Correction to the Eddy Forcing

According to Equations 6 and 8,  $\mathcal{D}_e$  should in theory augment the coarse-grid model toward  $\langle c \rangle$ . But as we apply  $\mathcal{D}_e$  calculated from Equation 8 in a coarse-grid simulation of the passive temperature tracer (i.e., let  $\mathcal{D} = \mathcal{D}_e$  in tracer Equation 6), the solution diverges from the  $\langle c \rangle$  after only 10 days. This is because  $\mathcal{D}_e$  has a complex spatial pattern and temporal variability, while its augmenting efficiency depends critically on its spatial and temporal relation to the large-scale flow. Even small errors in this relation can quickly grow leading to large local biases in the solution. A similar issue was reported by Berloff et al. (2021) in their PV eddy forcing.

To alleviate this deficiency, we re-ran the FULL\_EF experiment with additional relaxation of the solution toward the truth, saved the relaxation forcing, and added the resulting correction to the original  $\mathcal{D}_e$  to get a new eddy forcing  $\mathcal{D}_e^\dagger$ . The correction is verified to be small compared to the original  $\mathcal{D}_e$ , an area r.m.s. value of approximately 6%, but sufficient to suppress growing numerical errors. We confirmed that  $\mathcal{D}_e^\dagger$  is nearly identical to  $\mathcal{D}_e$ , and deviations due to the added relaxation forcing have an area r.m.s. value of about 6% of  $\mathcal{D}_e$ . We reran FULL\_EF with the new forcing  $\mathcal{D}_e^\dagger$  and no additional relaxation and confirmed that the solution indeed stays close to the truth with a relative difference of less than 1% (Figures B1a–B1c). We use the new eddy forcing for the whole analysis in this study, and we omit superscript “ $\dagger$ ” in the main text.

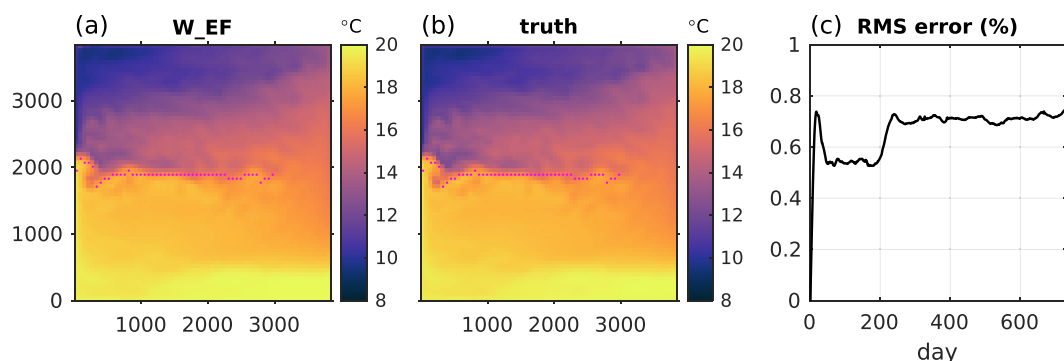


**Figure B1.** (a) The passive temperature solved in the FULL\_EF experiment. (b) The reference “true” tracer  $c_L$  (9) derived from high-resolution solution. (c) RMS value (multiplied by 100) of the relative error in the tracer in FULL\_EF (relative to the truth) versus time. Y-axis unit is [%]. Magenta dots are the jet core. All fields are in the upper layer.

### Appendix C: Statistics of the Diffusivity $\kappa$

We estimate the eddy diffusivity  $\kappa$  by inverting framework (Equation 14) with the eddy forcing from eight idealized tracers at each time step. Figure C1a shows the histogram over 2 years across the upper layer, and Figure C1b is a snapshot of  $\kappa$ . It is clear that  $\kappa$  has both prevalent positive and negative values and complex spatial distribution (Haigh et al., 2021b; Kamenkovich et al., 2021; Lu et al., 2022). For simplicity, when implementing

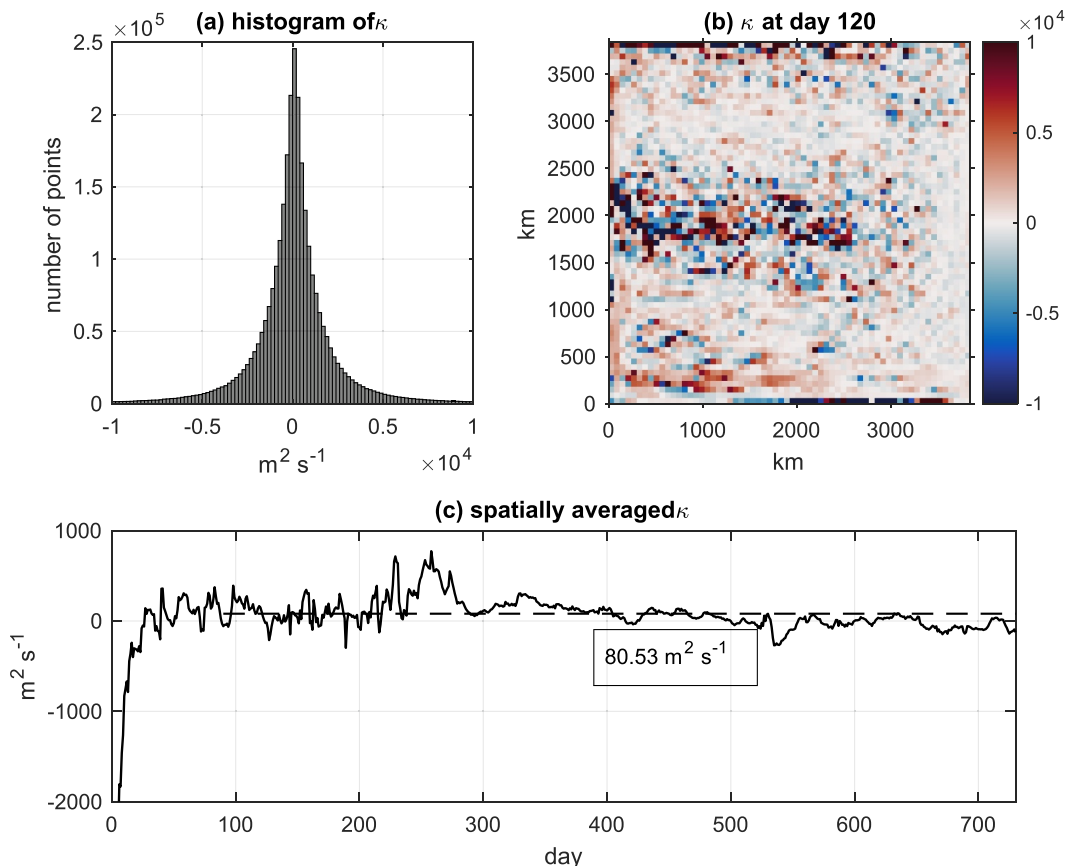


**Figure C1.** Statistics of  $\kappa(x, y, t)$  over-determined using the eight idealized tracers. (a) Histogram of  $\kappa$  across the domain over 2 years. (b) Snapshot of  $\kappa$  at day 120, year 21. (c) Time series of the domain-mean  $\kappa$ . The horizontal dashed line is a time average from day 90 years 21 to the end of year 22, and the box shows the value. Data are in the upper layer.

the framework we set  $\kappa$  as the space and time averaged value  $\kappa = 80 \text{ m}^2 \text{s}^{-1}$  (Figure C1c). This relatively small mean value is a result of cancellation between opposite-signed diffusivities, because of the significant spatial-temporal variation with both opposite-signed values in  $\kappa$ .

### Appendix D: Tracer Mass Conservation

To ensure the tracer conservation when applying the EEIV formulation (14), we add a correction to the local parameterized eddy forcing  $\hat{D}$  (Lu et al., 2022). The tracer solution  $c_*$  at a certain time step is given by

$$c_* = c_0 + \hat{D} \Delta t + w[\hat{D}] \Delta t, \quad (\text{D1})$$

$$w = -\frac{|\hat{D}|}{[|\hat{D}|]} \quad (\text{D2})$$

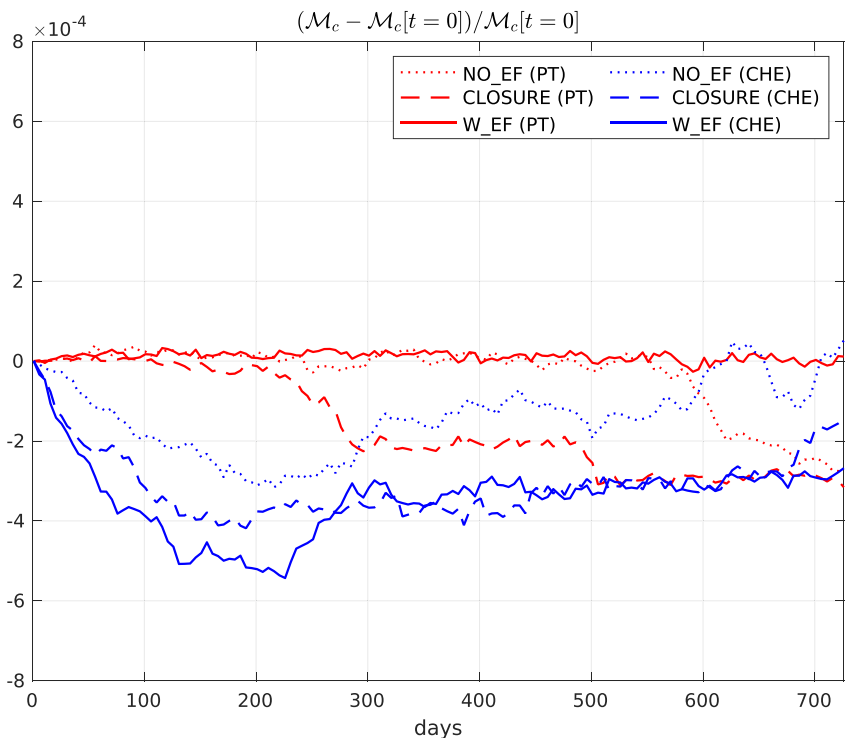


**Figure D1.** Evolution of the changes in the integrated tracer mass relative to the initial value from different experiments in the upper layer. Red is for the passive temperature tracer and blue is for the chemical tracer.

where  $c_0$  is the tracer at the last time step, the square brackets denote a global average of the layer thickness-weighted quantity:  $[A] = \int Ah \, dx dy / \int h \, dx dy$ , and the local weights  $w$  make the magnitude of the correction proportional to the amplitude of the local eddy forcing.

Tracer mass conservation requires  $[c_*] = [c_0]$ , which is satisfied by our choice of  $w$  above. One can prove this by taking  $\dots$  of D1. Note that Lu et al. (2022) chose a simpler weight  $w = 1$ , which was also tested in this study and did not affect our conclusions. Such correction that modifies the parameterized forcing has been widely applied to stochastic parameterizations in the operational ECMWF models (e.g., Leutbecher et al., 2017).

We present the changes of the globally integrated tracer inventory,  $M_c = \int ch \, dx dy$ , relative to its initial value for both the passive temperature and chemical tracers in Figure D1. The change in  $M_c$  from the IDL\_EEIV and FUN\_EEIV experiments remain in the same range (<0.1%) with that from the NO\_EF and FULL\_EF runs, confirming that the foregoing conservation modification works. Note that the total tracer inventory is not strictly conserved because of the relaxation surface boundary conditions, although such enforcement is straightforward to implement if desired (Lu et al., 2022).

## Data Availability Statement

The source code of the MOM6 ocean model configured for this study is available at <https://doi.org/10.5281/zenodo.14263240>. The offline tracer model source code and analysis code are available at <https://doi.org/10.5281/zenodo.14263244>. The offline tracer model outputs and diagnostics are available at <https://doi.org/10.5281/zenodo.10051655> (Lu & Kamenkovich, 2023).

## References

- Adcroft, A., Anderson, W., Balaji, V., Blanton, C., Bushuk, M., Dufour, C. O., et al. (2019). The GFDL Global Ocean and Sea Ice Model OM4.0: Model Description and Simulation Features. *Journal of Advances in Modeling Earth Systems*, 11(10), 3167–3211. <https://doi.org/10.1029/2019MS001726>
- Agarwal, N., Ryzhov, E., Kondrashov, D., & Berloff, P. (2021). Correlation-based flow decomposition and statistical analysis of the eddy forcing. *Journal of Fluid Mechanics*, 924, A5. <https://doi.org/10.1017/jfm.2021.604>

- Bachman, S. (2019). The GM+E closure: A framework for coupling backscatter with the Gent and McWilliams parameterization. *Ocean Modelling*, 136, 85–106. <https://doi.org/10.1016/j.ocemod.2019.02.006>
- Bachman, S., Fox-Kemper, B., & Bryan, F. (2015). A tracer-based inversion method for diagnosing eddy-induced diffusivity and advection. *Ocean Modelling*, 86, 1–14. <https://doi.org/10.1016/j.ocemod.2014.11.006>
- Bachman, S., Fox-Kemper, B., & Pearson, B. (2017). A scale-aware subgrid model for quasi-geostrophic turbulence. *Journal of Geophysical Research: Oceans*, 122(2), 1529–1554. <https://doi.org/10.1002/2016jc012265>
- Bachman, S. D., Fox-Kemper, B., & Bryan, F. O. (2020). A diagnosis of anisotropic eddy diffusion from a high-resolution global ocean model. *Journal of Advances in Modeling Earth Systems*, 12(2). <https://doi.org/10.1029/2019MS001904>
- Belkin, I., Cornillon, P., & Sherman, K. (2009). Fronts in large marine ecosystems. *Progress in Oceanography*, 81(1–4), 223–236. <https://doi.org/10.1016/j.pocean.2009.04.015>
- Berloff, P. (2005a). On dynamically consistent eddy fluxes. *Dynamics of Atmospheres and Oceans*, 38(3), 123–146. <https://doi.org/10.1016/j.dynatmoce.2004.11.003>
- Berloff, P. (2005b). Random-forcing model of the mesoscale oceanic eddies. *Journal of Fluid Mechanics*, 529, 71–95. <https://doi.org/10.1017/s0022112005003393>
- Berloff, P. (2015). Dynamically consistent parameterization of mesoscale eddies. Part I: Simple model. *Ocean Modelling*, 87, 1–19. <https://doi.org/10.1016/j.ocemod.2014.12.008>
- Berloff, P. (2018). Dynamically consistent parameterization of mesoscale eddies. Part III: Deterministic approach. *Ocean Modelling*, 127, 1–15. <https://doi.org/10.1016/j.ocemod.2018.04.009>
- Berloff, P., & Kamenkovich, I. (2013). On spectral analysis of mesoscale eddies. part ii: Nonlinear analysis. *Journal of Physical Oceanography*, 43(12), 2528–2544. <https://doi.org/10.1175/jpo-d-12-0233.1>
- Berloff, P., Kamenkovich, I., & Pedlosky, J. (2009). A model of multiple zonal jets in the oceans: Dynamical and kinematical analysis. *Journal of Physical Oceanography*, 39(11), 2711–2734. <https://doi.org/10.1175/2009JPO4093.1>
- Berloff, P., Ryzhov, E., & Shevchenko, I. (2021). On dynamically unresolved oceanic mesoscale motions. *Journal of Fluid Mechanics*, 920, A41. <https://doi.org/10.1017/jfm.2021.477>
- Capet, X., McWilliams, J. C., Molemaker, M. J., & Shchepetkin, A. F. (2008). Mesoscale to submesoscale transition in the California current system. Part I: Flow structure, eddy flux, and observational tests. *Journal of Physical Oceanography*, 38(1), 29–43. <https://doi.org/10.1175/2007jpo3671.1>
- Cooper, F., & Zanna, L. (2015). Optimisation of an idealised ocean model, stochastic parameterisation of sub-grid eddies. *Ocean Modelling*, 88, 38–53. <https://doi.org/10.1016/j.ocemod.2014.12.014>
- D'Asaro, E., Lee, C., Rainville, L., Harcourt, R., & Thomas, L. (2011). Enhanced turbulence and energy dissipation at ocean fronts. *Science*, 332(6027), 318–322. <https://doi.org/10.1126/science.1201515>
- Dritschel, D. G., & McIntyre, M. E. (2008). Multiple jets as PV staircases: The Phillips effect and the resilience of eddy-transport barriers. *Journal of the Atmospheric Sciences*, 65(3), 855–874. <https://doi.org/10.1175/2007jas2227.1>
- Eden, C. (2006). Thickness diffusivity in the southern ocean. *Geophysical Research Letters*, 33(11). <https://doi.org/10.1029/2006gl026157>
- England, M. H., Garçon, V., & Minster, J. (1994). Chlorofluorocarbon uptake in a world ocean model: 1. Sensitivity to the surface gas forcing. *Journal of Geophysical Research*, 99(C12), 25215–25233. <https://doi.org/10.1029/94JC02205>
- Ferrari, R. (2011). A frontal challenge for climate models. *Science*, 332(6027), 316–317. <https://doi.org/10.1126/science.1203632>
- Gent, P., & McWilliams, J. (1990). Isopycnal mixing in ocean circulation models. *Journal of Physical Oceanography*, 20(1), 150–155. [https://doi.org/10.1175/1520-0485\(1990\)020<150:IMOCM>2.0.CO;2](https://doi.org/10.1175/1520-0485(1990)020<150:IMOCM>2.0.CO;2)
- Gent, P., Willebrand, J., McDougall, T., & McWilliams, J. (1995). Parameterizing eddy-induced tracer transports in ocean circulation models. *Journal of Physical Oceanography*, 25(4), 463–474. [https://doi.org/10.1175/1520-0485\(1995\)025<463:PEITI>2.0.CO;2](https://doi.org/10.1175/1520-0485(1995)025<463:PEITI>2.0.CO;2)
- Griffies, S. M., & Hallberg, R. W. (2000). Biharmonic friction with a smagorinsky-like viscosity for use in large-scale eddy-permitting ocean models. *Monthly Weather Review*, 128(8), 2935–2946. [https://doi.org/10.1175/1520-0493\(2000\)128<2935:BFWASL>2.0.CO;2](https://doi.org/10.1175/1520-0493(2000)128<2935:BFWASL>2.0.CO;2)
- Grooms, I. (2016). A Gaussian-product stochastic Gent–McWilliams parameterization. *Ocean Modelling*, 106, 27–43. <https://doi.org/10.1016/j.ocemod.2016.09.005>
- Grooms, I. (2023). Backscatter in energetically-constrained Leith parameterizations. *Ocean Modelling*, 186, 102265. <https://doi.org/10.1016/j.ocemod.2023.102265>
- Grooms, I., & Kleiber, W. (2019). Diagnosing, modeling, and testing a multiplicative stochastic Gent–McWilliams parameterization. *Ocean Modelling*, 133, 1–10. <https://doi.org/10.1016/j.ocemod.2018.10.009>
- Grooms, I., Majda, A. J., & Smith, K. S. (2015). Stochastic superparameterization in a quasigeostrophic model of the Antarctic circumpolar current. *Ocean Modelling*, 85, 1–15. <https://doi.org/10.1016/j.ocemod.2014.10.001>
- Guillaumin, A., & Zanna, L. (2021). Stochastic-deep learning parameterization of ocean momentum forcing. *Journal of Advances in Modeling Earth Systems*, 13(9), e2021MS002534. <https://doi.org/10.1029/2021MS002534>
- Haigh, M., & Berloff, P. (2021). On co-existing diffusive and anti-diffusive tracer transport by oceanic mesoscale eddies. *Ocean Modelling*, 168, 101909. <https://doi.org/10.1016/j.ocemod.2021.101909>
- Haigh, M., & Berloff, P. (2022). On the stability of tracer simulations with opposite-signed diffusivities. *Journal of Fluid Mechanics*, 937, R3. <https://doi.org/10.1017/jfm.2022.126>
- Haigh, M., Sun, L., McWilliams, J., & Berloff, P. (2021a). On eddy transport in the ocean. Part II: The advection tensor. *Ocean Modelling*, 165, 101845. <https://doi.org/10.1016/j.ocemod.2021.101845>
- Haigh, M., Sun, L., McWilliams, J., & Berloff, P. (2021b). On eddy transport in the ocean. Part I: The diffusion tensor. *Ocean Modelling*, 164, 101831. <https://doi.org/10.1016/j.ocemod.2021.101831>
- Haigh, M., Sun, L., Shevchenko, I., & Berloff, P. (2020). Tracer-based estimates of eddy-induced diffusivities. *Deep Sea Res. I: Oceanographic Research Papers*, 160, 103264. <https://doi.org/10.1016/j.dsr.2020.103264>
- Haney, R. (1971). Surface thermal boundary condition for ocean circulation models. *Journal of Physical Oceanography*, 1(4), 241–248. [https://doi.org/10.1175/1520-0485\(1971\)001<241:STBCFO>2.0.CO;2](https://doi.org/10.1175/1520-0485(1971)001<241:STBCFO>2.0.CO;2)
- Hewitt, H. e. a., Roberts, M., Mathiot, P., Biastoch, A., Blockley, E., Chassignet, E. P., et al. (2020). Resolving and parameterising the ocean mesoscale in Earth system models. *Current Climate Change Reports*, 6(4), 137–152. <https://doi.org/10.1007/s40641-020-00164-w>
- Holmes, R., Groeskamp, S., Stewart, K., & McDougall, T. (2022). Sensitivity of a coarse-resolution global ocean model to a spatially variable neutral diffusivity. *Journal of Advances in Modeling Earth Systems*, 14(3), e2021MS002914. <https://doi.org/10.1029/2021ms002914>
- Hoskins, B. (1982). The mathematical theory of frontogenesis. *Annual Review of Fluid Mechanics*, 14(1), 131–151. <https://doi.org/10.1146/annurev.fl.14.010182.001023>

- Jansen, M. F., Adcroft, A., Khani, S., & Kong, H. (2019). Toward an energetically consistent, resolution aware parameterization of ocean mesoscale eddies. *Journal of Advances in Modeling Earth Systems*, 11(8), 2844–2860. <https://doi.org/10.1029/2019ms001750>
- Jansen, M. F., & Held, I. M. (2014). Parameterizing subgrid-scale eddy effects using energetically consistent backscatter. *Ocean Modelling*, 80, 36–48. <https://doi.org/10.1016/j.ocemod.2014.06.002>
- Kamenkovich, I., Berloff, P., Haigh, M., Sun, L., & Lu, Y. (2021). Complexity of mesoscale eddy diffusivity in the ocean. *Geophysical Research Letters*, 48(5). <https://doi.org/10.1029/2020GL091719>
- Kamenkovich, I., Berloff, P., & Irina, R. (2019). Anisotropic and inhomogeneous eddy-induced transport in flows with jets. In *Zonal jets: Phenomenology, genesis, and physics* (pp. 437–449). Cambridge University Press.
- Kamenkovich, I., & Garraffo, Z. (2022). Importance of mesoscale currents in Amoc pathways and timescales. *Journal of Physical Oceanography*, 52(8), 1613–1628. <https://doi.org/10.1175/JPO-D-21-0244.1>
- Kamenkovich, I., Garraffo, Z., Pennel, R., & Fine, R. (2017). Importance of mesoscale eddies and mean circulation in ventilation of the Southern Ocean. *Journal of Geophysical Research: Oceans*, 122(4), 2724–2741. <https://doi.org/10.1002/2016JC012292>
- Kirtman, B. e. a., Bitz, C., Bryan, F., Collins, W., Dennis, J., Hearn, N., et al. (2012). Impact of ocean model resolution on CCSM climate simulations. *Climate Dynamics*, 39(6), 1303–1328. <https://doi.org/10.1007/s00382-012-1500-3>
- Leutbecher, M. e. a., Lock, S., Ollinaho, P., Lang, S. T. K., Balsamo, G., Bechtold, P., et al. (2017). Stochastic representations of model uncertainties at ECMWF: State of the art and future vision. *Quarterly Journal of the Royal Meteorological Society*, 143(707), 2315–2339. <https://doi.org/10.1002/qj.3094>
- Li, Q., & Lee, S. (2017). A mechanism of mixed layer formation in the Indo–western Pacific Southern Ocean: Preconditioning by an eddy-driven jet-scale overturning circulation. *Journal of Physical Oceanography*, 47(11), 2755–2772. <https://doi.org/10.1175/JPO-D-17-0006.1>
- Li, Q., Lee, S., & Griesel, A. (2016). Eddy fluxes and jet-scale overturning circulations in the Indo–western Pacific Southern Ocean. *Journal of Physical Oceanography*, 46(10), 2943–2959. <https://doi.org/10.1175/JPO-D-15-0241.1>
- Lohmann, R., & Belkin, I. (2014). Organic pollutants and ocean fronts across the Atlantic Ocean: A review. *Progress in Oceanography*, 128, 172–184. <https://doi.org/10.1016/j.pocean.2014.08.013>
- Lu, Y., & Kamenkovich, I. (2023). Dataset for “mesoscale eddy-induced sharpening of oceanic tracer front” [dataset]. Zenodo. <https://doi.org/10.5281/zenodo.10051655>
- Lu, Y., Kamenkovich, I., & Berloff, P. (2022). Properties of the lateral mesoscale eddy-induced transport in a high-resolution ocean model: Beyond the flux-gradient relation. *Journal of Physical Oceanography*, 52(12), 3273–3295. <https://doi.org/10.1175/JPO-D-22-0108.1>
- Maddison, J., Marshall, D., & Shipton, J. (2015). On the dynamical influence of ocean eddy potential vorticity fluxes. *Ocean Modelling*, 92, 169–182. <https://doi.org/10.1016/j.ocemod.2015.06.003>
- Manz, P., & Zanna, L. (2014). Toward a stochastic parameterization of ocean mesoscale eddies. *Ocean Modelling*, 79, 1–20. <https://doi.org/10.1016/j.ocemod.2014.04.002>
- Marques, G. M., Loose, N., Yankovsky, E., Steinberg, J. M., Chang, C.-Y., Bhamidipati, N., et al. (2022). Neverworld2: An idealized model hierarchy to investigate ocean mesoscale eddies across resolutions. *Geoscientific Model Development*, 15(17), 6567–6579. <https://doi.org/10.5194/gmd-15-6567-2022>
- Marshall, J., & Shutts, G. (1981). A note on rotational and divergent eddy fluxes. *Journal of Physical Oceanography*, 11(12), 1677–1680. [https://doi.org/10.1175/1520-0485\(1981\)011\(1677:ANORAD\)2.0.CO;2](https://doi.org/10.1175/1520-0485(1981)011(1677:ANORAD)2.0.CO;2)
- McWilliams, J. (2016). Submesoscale currents in the ocean. *Proceedings of the Royal Society A: Mathematical, Physical and Engineering Sciences*, 472(2189), 20160117. <https://doi.org/10.1098/rspa.2016.0117>
- McWilliams, J. (2021). Oceanic frontogenesis. *Annual Review of Fluid Mechanics*, 13(1), 227–253. <https://doi.org/10.1146/annurev-marine-032320-120725>
- Meijers, A. (2014). The Southern Ocean in the Coupled Model Intercomparison Project phase 5. *Philosophical Transactions of the Royal Society A*, 372(2019), 20130296. <https://doi.org/10.1098/rsta.2013.0296>
- Minobe, S., Kuwano-Yoshida, A., Komori, N., Xie, S.-P., & Small, J. (2008). Influence of the Gulf Stream on the troposphere. *Nature*, 452(7184), 206–209. <https://doi.org/10.1038/nature06690>
- Mudrick, S. (1974). A numerical study of frontogenesis. *Journal of the Atmospheric Sciences*, 31(4), 869–892. [https://doi.org/10.1175/1520-0469\(1974\)031\(0869:ansof\)2.0.co;2](https://doi.org/10.1175/1520-0469(1974)031(0869:ansof)2.0.co;2)
- Nakamura, N. (1996). Two-dimensional mixing, edge formation, and permeability diagnosed in an area coordinate. *Journal of the Atmospheric Sciences*, 53(11), 1524–1537. [https://doi.org/10.1175/1520-0469\(1996\)053\(1524:TDMEFA\)2.0.CO;2](https://doi.org/10.1175/1520-0469(1996)053(1524:TDMEFA)2.0.CO;2)
- Nakamura, N., & Zhu, D. (2010). Formation of jets through mixing and forcing of potential vorticity: Analysis and parameterization of beta-plane turbulence. *Journal of the Atmospheric Sciences*, 67(9), 2717–2733. <https://doi.org/10.1175/2009JAS3159.1>
- Parfitt, R., Czaja, A., Minobe, S., & Kuwano-Yoshida, A. (2016). The atmospheric frontal response to SST perturbations in the Gulf Stream region. *Geophysical Research Letters*, 43(5), 2299–2306. <https://doi.org/10.1002/2016gl067723>
- Partee, S., Ellis, M., Rigazzi, A., Shao, A., Bachman, S., Marques, G., & Robbins, B. (2022). Using Machine Learning at scale in numerical simulations with SmartSim: An application to ocean climate modeling. *Journal of Computer Science*, 62, 101707. <https://doi.org/10.1016/j.jocs.2022.101707>
- Patching, S. (2022). On divergence- and gradient-preserving coarse-graining for finite volume primitive equation ocean models. *Ocean Modelling*, 170, 101941. <https://doi.org/10.1016/j.ocemod.2021.101941>
- Pedlosky, J. (1987). *Geophysical fluid dynamics*. Springer.
- Perezhogin, P., Zanna, L., & Fernandez-Granda, C. (2023). Generative data-driven approaches for stochastic subgrid parameterizations in an idealized ocean model. *Journal of Advances in Modeling Earth Systems*, 15(10), e2023MS003681. <https://doi.org/10.1029/2023ms003681>
- Redi, M. (1982). Oceanic isopycnal mixing by coordinate rotation. *Journal of Physical Oceanography*, 12(10), 1154–1158. [https://doi.org/10.1175/1520-0485\(1982\)012\(1154:OIMBCR\)2.0.CO;2](https://doi.org/10.1175/1520-0485(1982)012(1154:OIMBCR)2.0.CO;2)
- Rhines, P. B., & Young, W. R. (1982). Homogenization of potential vorticity in planetary gyres. *Journal of Fluid Mechanics*, 122(-1), 347–367. <https://doi.org/10.1017/S0022112082002250>
- Ross, A., Li, Z., Perezhogin, P., Fernandez-Granda, C., & Zanna, L. (2023). Benchmarking of machine learning ocean subgrid parameterizations in an idealized model. *Journal of Advances in Modeling Earth Systems*, 15(1), e2022MS003258. <https://doi.org/10.1029/2022MS003258>
- Rypina, I., Jayne, S., Yoshida, S., Macdonald, A. M., Douglass, E., & Buesseler, K. (2013). Short-term dispersal of Fukushima-derived radionuclides off Japan: Modeling efforts and model-data intercomparison. *Biogeosciences*, 10(7), 4973–4990. <https://doi.org/10.5194/bg-10-4973-2013>
- Rypina, I., Pratt, L., & Lozier, S. (2011). Near-surface transport pathways in the north Atlantic Ocean: Looking for throughput from the subtropical to the subpolar gyre. *Journal of Physical Oceanography*, 41(5), 911–925. <https://doi.org/10.1175/2011JPO4498.1>

- Ryzhov, E., & Berloff, P. (2022). On transport tensor of dynamically unresolved oceanic mesoscale eddies. *Journal of Fluid Mechanics*, 939, A7. <https://doi.org/10.1017/jfm.2022.169>
- Seo, H. e. a., O'Neill, L. W., Bourassa, M. A., Czaja, A., Drushka, K., Edson, J. B., et al. (2023). Ocean mesoscale and frontal-scale ocean-atmosphere interactions and influence on large-scale climate: A review. *Journal of Climate*, 36(7), 1981–2013. <https://doi.org/10.1175/jcli-d-21-0982.1>
- Shevchenko, I., & Berloff, P. (2015). Multi-layer quasi-geostrophic ocean dynamics in Eddy-resolving regimes. *Ocean Modelling*, 94, 1–14. <https://doi.org/10.1016/j.ocemod.2015.07.018>
- Siqueira, L., & Kirtman, B. (2016). Atlantic near-term climate variability and the role of a resolved Gulf Stream. *Geophysical Research Letters*, 43(8), 3964–3972. <https://doi.org/10.1002/2016gl068694>
- Small, J., deSzoeke, S., Xie, S., O'Neill, L., Seo, H., Song, Q., et al. (2008). Air-sea interaction over ocean fronts and eddies. *Dynamics of Atmospheres and Oceans*, 45(3–4), 274–319. <https://doi.org/10.1016/j.dynatmoce.2008.01.001>
- Small, J., Tomas, R., & Bryan, F. (2014). Storm track response to ocean fronts in a global high-resolution climate model. *Climate Dynamics*, 43(3), 805–828. <https://doi.org/10.1007/s00382-013-1980-9>
- Sun, L., Haigh, M., Shevchenko, I., Berloff, P., & Kamenkovich, I. (2021). On non-uniqueness of the mesoscale eddy diffusivity. *Journal of Fluid Mechanics*, 920, A32. <https://doi.org/10.1017/jfm.2021.472>
- Trias, F., Dabbagh, F., Gorobets, A., & Oliet, C. (2020). On a proper tensor-diffusivity model for large-eddy simulation of buoyancy-driven turbulence. *Flow, Turbulence and Combustion*, 105(2), 393–414. <https://doi.org/10.1007/s10494-020-00123-3>
- Uchida, T., Dereimble, B., & Popinet, S. (2022). Deterministic model of the eddy dynamics for a midlatitude ocean model. *Journal of Physical Oceanography*, 52(6), 1133–1154. <https://doi.org/10.1175/JPO-D-21-0217.1>
- Vallis, G. K. (2017). *Atmospheric and oceanic fluid dynamics*. Cambridge University Press.
- Wang, P., Yuval, J., & O'Gorman, P. A. (2022). Non-local parameterization of atmospheric subgrid processes with neural networks. *Journal of Advances in Modeling Earth Systems*, 14(10), e2022MS002984. <https://doi.org/10.1029/2022ms002984>
- Waterman, S., Hogg, N., & Jayne, S. (2011). Eddy-mean flow interaction in the Kuroshio extension region. *Journal of Physical Oceanography*, 41(6), 1182–1208. <https://doi.org/10.1175/2010JPO4564.1>
- Waterman, S., & Jayne, S. (2011). Eddy-mean flow interactions in the along-stream development of a western boundary current jet: An idealized model study. *Journal of Physical Oceanography*, 41(4), 682–707. <https://doi.org/10.1175/2010JPO4477.1>
- Yankovsky, E., Bachman, S. D., Smith, K. S., & Zanna, L. (2024). Vertical structure and energetic constraints for a backscatter parameterization of ocean mesoscale eddies. *Journal of Advances in Modeling Earth Systems*, 16(7). <https://doi.org/10.1029/2023MS004093>
- Yankovsky, E., Zanna, L., & Smith, S. (2022). Influences of mesoscale ocean eddies on flow vertical structure in a resolution-based model hierarchy. *Journal of Advances in Modeling Earth Systems*, 14(11), e2022MS003203. <https://doi.org/10.1029/2022MS003203>
- Yuval, J., & O'Gorman, P. A. (2023). Neural-network parameterization of subgrid momentum transport in the atmosphere. *Journal of Advances in Modeling Earth Systems*, 15(4), e2023MS003606. <https://doi.org/10.1029/2023ms003606>
- Zanna, L., & Bolton, T. (2020). Data-driven equation discovery of ocean mesoscale closures. *Geophysical Research Letters*, 47(17), e2020GL088376. <https://doi.org/10.1029/2020GL088376>
- Zanna, L., Mana, P., Anstey, J., David, T., & Bolton, T. (2017). Scale-aware deterministic and stochastic parametrizations of eddy-mean flow interaction. *Ocean Modelling*, 111, 66–80. <https://doi.org/10.1016/j.ocemod.2017.01.004>
- Zhang, C., Perezhogin, P., Gultekin, C., Adcroft, A., Fernandez-Granda, C., & Zanna, L. (2023). Implementation and evaluation of a machine learned mesoscale eddy parameterization into a numerical ocean circulation model. *Journal of Advances in Modeling Earth Systems*, 15(10), e2023MS003697. <https://doi.org/10.1029/2023MS003697>
- Zhang, W., & Wolfe, C. (2022). On the vertical structure of oceanic mesoscale tracer diffusivities. *Journal of Advances in Modeling Earth Systems*, 14(6). <https://doi.org/10.1029/2021MS002891>